Rapid plasmonic actuation of thermoresponsive hydrogel structures

DIPLOMA THESIS

submitted in partial fulfillment of the requirements for the degree of

Diplom-Ingenieurin (Dipl.-Ing.^{in})

in

Biomedical Engineering

by

Simone Katharina Auer, BSc.

Registration Number 01406722

to the Faculty of Electrical Engineering and Information Technology
of the Vienna University of Technology

Supervisors: Dr. Jakub Dostalek
Dr.in techn. Dipl.-Ing. Ioanna Giouroudi

Vienna, 12th September 2022

Schnelle plasmonische Aktivierung thermoresponsiver Hydrogelstrukturen

DIPLOMARBEIT

Zur Erlangung des akademischen Grades

Diplom-Ingenieurin (Dipl.-Ing.^{in})

Im Rahmen des Studiums

Biomedical Engineering

eingereicht von

Simone Katharina Auer, BSc.

Matrikelnummer 01406722

an der Fakultät für Elektrotechnik und Informationstechnik
der Technischen Universität Wien

Betreuung: Dr. Jakub Dostalek
Dr.in techn. Dipl.-Ing. Ioanna Giouroudi

Wien, 12. September 2022

Affidavits

I declare that I have written this thesis independently, that I have not used any sources or resources other than those indicated and that I have expressly identified all sources quoted verbatim or in terms of content from the sources used.

Eidesstattliche Erklärung

Ich erkläre hiermit, dass ich diese Arbeit selbstständig verfasst, keine anderen als die angegebenen Quellen und Hilfsmittel benutzt und alle wörtlich oder inhaltlich zitierten Quellen ausdrücklich von den verwendeten Quellen gekennzeichnet habe.

_____

Simone Katharina Auer, 12th September 2022

Acknowledgements

First of all, I would like to thank my supervisor and group leader Dr. Jakub Dostalek. Joining his research group opened my way to science and I am truly grateful to have learned under his guidance which eventually made me want to stay on this path.

I also want to thank my supervisor from TU Vienna Dr.in techn. Dipl.-Ing. Ioanna Giouroudi for her time and work to make this thesis feasible.

Furthermore, I am thanking Stefan Fossati, who taught me everything to get started in the lab and never got tired of explaining and discussing any imaginable question. In this way, I would also like to thank my incredible colleagues, especially Detti, Chiara, Anil, Jakob, Ciril and Uli from the BioSensor Technology group at AIT, who have prompted me to extend my 2-month internship to almost 4 years, and whom I somehow can't seem to leave.

From all my heart, I am beyond grateful to my family, my beloved sister Meggi, my grandmother Sigrid, my father and stepmother Michael and Conni, and in particular my mother Sabine for supporting me with endless love and believe in me. And finally, with all my love, I am thanking my partner Gonzalo who stood by my side with never ending patience, laughing support in times of desperation and truly helpful advice during all this time.

♡

Abstract

Poly (N-isopropylacrylamide) (pNIPAAm) is a thermoresponsive polymer that is often used as functional material in soft robotics, as well as biocompatible, adaptable, and external tunable compound in many biomedical applications. Crosslinked and exposed to water, pNIPAAm can form soft hydrogels with a lower critical solution temperature (LCST) of 32 °C above which they undergo a phase transition from a swollen, hydrophilic to a collapsed, hydrophobic state. In this work, the kinetics of the swelling and collapsing process of such pNIPAAm based polymer networks are investigated under various external conditions in the millisecond time range.

For this purpose, a thin layer (∼ 800 nm in the swollen state) of pNIPAAm based hydrogel is attached to a substrate with arrays of plasmonic nanoparticles (NPs). Their localized surface plasmon resonances (LSPRs) are used for rapid and local plasmonic heating and simultaneous time-resolved monitoring of the gel with an inhouse developed optical system.

The state transition is studied for increasing heating strength, varying ambient temperature before the actuation of the transition and for different heating durations. The results reveal that the dependence of the transition kinetics on the external parameters for the swelling and the collapse are different. While the collapse time is minimized to 3.2 and 1.5 ms with increasing heating intensity and ambient temperature respectively, the swelling shows to be more independent of the previously applied temperature difference. However, two consecutive phases evolve for the swelling process, when the network is preconditioned close to the LCST by elevated ambient temperature, with an increasing first phase of slow swelling, which delays the second actual process of exponential swelling by up to 20 ms. Furthermore, with longer heating durations, another superimposed transition process with a time constant of > 20 ms is found for the collapse, which was not observed before in similar experiments with pNIPAAM polymer brushes.

These observations could contribute to a better understanding of the widely used material and thereby benefit the design and development of new devices in the field of biomedical engineering and soft micro-machines and -robotics.

Kurzfassung

Poly (N-Isopropylacrylamid) (pNIPAAm) ist ein thermoresponsives Polymer, das vielmals als funktionelles Material in der Soft-Robotik und als biokompatible, adaptionsfähige und extern steuerbare Komponente in vielen biomedizinischen Anwendungen verwendet wird. Vernetzt und Wasser ausgesetzt, kann pNIPAAm weiche Hydrogele mit einer unteren kritischen Lösungstemperatur (LCST) von 32 °C bilden, oberhalb derer sie einen Phasenübergang von einem gequollenen, hydrophilen zu einem kollabierten, hydrophoben Zustand durchlaufen.

In dieser Arbeit wird die Kinetik des Quell- und Kollabierprozesses solcher pNIPAAm-basierten Polymernetzwerke unter verschiedenen äußeren Bedingungen im Millisekundenbereich untersucht.

Zu diesem Zweck wird eine dünne Schicht (~800 nm Dicke im gequollenen Zustand) aus pNIPAAm-basiertem Hydrogel auf ein Substrat mit Arrays aus plasmonischen Nanopartikeln (NPs) aufgetragen. Deren lokalisierte Oberflächenplasmonenresonanzen (LSPRs) werden verwendet, um das Gel schnell und lokal, plasmonische zu erwärmen und es gleichzeitig zeitaufgelöst mit einem selbst entwickelten optischen System beobachten zu können.

Der Zustandsübergang wird für zunehmende Heizleistung, variierende Umgebungstemperatur vor Aktivierung des Übergangs und für unterschiedliche Heizdauern untersucht. Die Ergebnisse zeigen, dass die Abhängigkeit der Übergangskinetik von den äußeren Parametern für Quellung und Kollaps unterschiedlich sind. Während die Kollabierzeit mit zunehmender Heizintensität bzw. Umgebungstemperatur auf 3,2 bzw. 1,5 ms minimiert wird, ist die Quellung unabhängiger von der zuvor angelegten Temperaturdifferenz. Wenn jedoch das Netzwerk in der Nähe der LCST durch erhöhte Umgebungstemperatur vorkonditioniert wird, entwickeln sich für den Quellvorgang zwei aufeinanderfolgende Phasen mit einer zunehmenden ersten Phase langsamen Quellens, die den zweiten eigentlichen Prozess des exponentiellen Quellens um bis zu 20 ms verzögert. Darüber hinaus findet sich bei längeren Heizdauern ein weiterer überlagerter Übergangsprozess mit einer Zeitkonstante von > 20 ms für den Kollaps, der zuvor in ähnlichen Experimenten mit pNIPAAM-Polymerbürsten nicht beobachtet wurde.

Diese Beobachtungen könnten zu einem besseren Verständnis dieses weit verbreiteten Materials beitragen und somit dem Design und der Entwicklung neuer Errungenschaften auf dem Gebiet der biomedizinischen Technik, der weichen Mikromaschinen und -robotik zugutekommen.

Table of Content

1. Introduction

1.1 Polymer networks

Polymer networks are 3D structures composed of polymers crosslinked either by physical interactions (e.g., Van der Waals, hydrophobic, or Coulomb interactions), or by chemical means (e.g., covalent binding). Depending on the composition and arrangement of the polymer chains and the crosslinking nodes, these networks can offer a wide variety of interesting properties, such as adaptable elasticity, tunable mechanical strength, porosity, or even the ability to swell. Despite the high variability, polymer networks can be divided into basically four big subgroups: Thermosets, Thermoplastics, Elastomers and Gels. *Thermosets*, like formaldehyde or epoxy resins, are rigid, covalently bound polymer networks which are not further processable or deformable once they are hardened. *Thermoplastics*, on the other hand, are based on non-covalent, supramolecular bonds and, even though these materials are rather rigid and firm, they turn into a viscoelastic liquid when heated, and they can therefore be deformed, recycled, or restored. Examples for thermoplastics are Acrylonitrile Butadiene Styrene (ABS) as manufacturing material for LEGO (www.lego.com) [1], or polyamides as Nylon. *Elastomers* like vulcanized natural rubber or silicon rubbers are mostly covalently bonded and are soft materials which hold high elastic properties. Finally, *polymeric gels* are very soft and highly deformable polymer networks. They are held together either covalently or non-covalently and, when embedded in liquids such as water or organic solvents, the network structure retains the liquid and the gel swells.[2] Next, if the gel swells in water, it is called a hydrogel.[3] The strong affinity to water of these materials is provided by hydrophilic functional groups, as for example hydroxyl, amino, carboxyl or ionic moieties.[4,5]

1.2 Responsive hydrogels

By choosing the polymer, hydrogels can be made responsive to different *stimuli* such as pH[6], ionic strength[7], irradiation[8], or temperature[9]. Moreover, it is also possible to combine polymers that respond to different stimuli in multi-responsive gels, where they can either

compete or support each other[10,11]. The external stimulation creates a shift in the molecular balance of hydrophilicity and hydrophobicity in the polymer chains, which induces a phase transition of the network and results in volume or shape changes in the form of swelling or shrinkage throughout the material. For temperature-sensitive hydrogels, the turning point for this change of state is characterized by a lower or upper critical solution temperature (LCST or UCST), respectively. There, a network transition from a hydrophilic swollen to a hydrophobic collapsed state occurs above the LCST, or below the UCST, and before absorbed water is released.[4]

1.3 Poly (N-isopropylacrylamide) (pNIPAAm)

A considerably well studied hydrogel sensitive to temperature changes is that based on poly (N-isopropylacrylamide) (pNIPAAm)[12–15]. Shown in **Figure 1**, this polymer has the acrylamide substituted by an isopropyl group at its nitrogen[15,16].

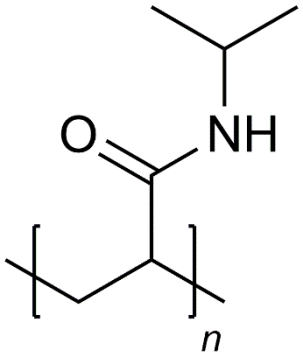

Figure 1. *Chemical structure of pNIPAAm.*

This hydrogel is characterized by a lower critical solution temperature (LCST) of about 32° C, above which it undergoes the volume phase transition from a swollen to a collapsed state [12,17]. Below the LCST, the pNIPAAm-based network shows an open, water-exposed conformation as the hydrophilic amide-water hydrogen bonds overcome the contribution of the hydrophobic isopropyl groups. The swollen structure is stabilized by hydrate shells formed at the amide bonds. When heated up above its LCST, the hydrogen bonds, which are stabilizing the water clusters, are disrupted and the thermal excitation loosens the hydrogen bonds at the C=O, which is adding up to the hydrophobicity and thereby eventually outweighing the impact of the hydrophilic amide bond. Consequently, the structure of the pNIPAAm network is shrinking to a compact conformation (see **Figure 2**),

minimizing the interface to the water-accessible hydrophobic parts of the isopropyl by a collapse of the whole network, and thereby expelling water [18].

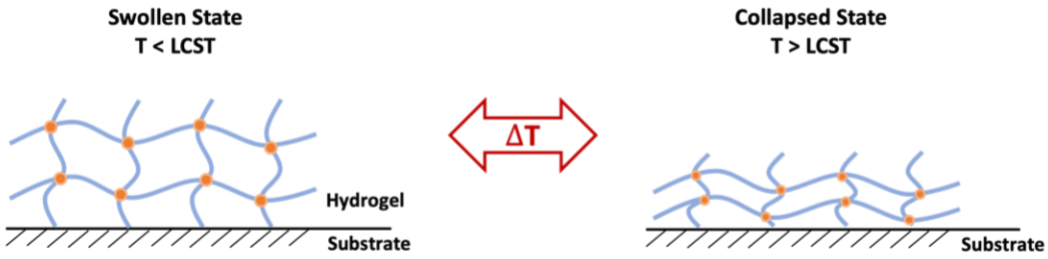

Figure 2. *Sketch of the collapse of a surface tethered hydrogel structure after temperature increase above the LCST [adapted from [19]].*

Due to the LCST value of pNIPAAm close to the human body temperature, as well as its biocompability and softness, and the reversible actuation of the phase transition, this material is very attractive in a wide range of fields, as especially in the biomedical area. Therefore, it has emerged as one of the most used thermoresponsive materials[19], showing applications in thermally controlled drug delivery systems where, for example, pNIPAAm-containing micelles open to release their load at assigned sites at a specific temperature for e.g. targeted cancer treatment[20]. Furthermore, pNIPAAm-based networks have also been employed in biosensing applications as analyte-binding matrix for signal amplification[21] or as a tool in tissue engineering and reconstruction as cell culture surfaces for myocardial cell tissue[22].

1.4 Response time of thermoresponsive hydrogel structures

In applications that utilize thermoresponsive hydrogel architectures, the response time of the polymer structure to the temperature changes plays a significant role and is therefore of high interest. For instance, pNIPAAm based hydrogel was employed in thermally actuatable valves of microfluidic devices, which allows reversible switching between their opened and closed state within 5 s.[23] In another example thin pNIPAAm structures consisting micro ribbons were developed, which can run through motion sequences arising from optically stimulated shape transformations within 1s, as can be followed in **Figure 3**.[9]

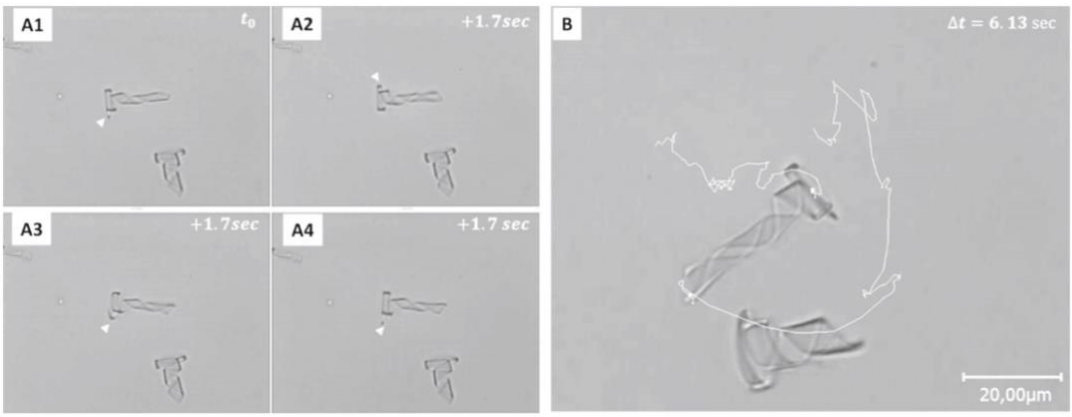

Figure 3. *Locomotion of a pNIPAAM based hydrogel ribbon driven by shape transformation within seconds: A1 – A4 show a sequence of images taken every 1.7 s, where the ribbons where repeatedly actuated with 200* ***µ****s long NIR-pulses, which led to a counter-clockwise spin around the helical axis; B shows the trajectory after 6.13 s: the spin of the ribbon resulted in a clockwise rotation of the whole micro swimmer [reproduced from* [9]*].*

The phase transition duration of the polymer structures depends, among other things, on how quickly both the individual chains and the collective system of them can react to temperature variations in the form of conformational changes and how well water molecules can diffuse through the network.

1.5 Thermal excitation of responsive hydrogels – Plasmonic Heating

A possibility to thermally stimulate responsive polymer structures on a millisecond time range is offered by the effect of *plasmonic heating*, where heat is generated by specifically irradiating incorporated metallic nanoparticles. It offers a reversible, rapid, and locally acting alternative [24] to the use of Peltier elements [25] or ITO micro heaters [26], which are suitable for rather inert heating of macroscopic volumes.[27]

In general, when illuminating a single metallic nanoparticle (NP), one part of the incoming radiation gets scattered and the other one absorbed [28]. At resonant irradiation (λ_{LSPR}), the absorbed energy excites localized surface plasmons (LSPs) by coupling to the electron density oscillations in the metal and also generates heat due to Ohmic losses, as depicted in **Figure 4**. Therefore, resonantly illuminated metallic NPs can act as nano-heat sources that locally increase the temperature in their vicinity.

The heating power q, generated by a single NP, is depending on its absorption cross-section σ_{abs} and the irradiation intensity I:

$$q = \sigma_{abs} I \, . \tag{1}$$

The produced heat leads to a temperature increase ΔT in the surrounding medium with thermal conductivity κ:

$$\Delta T = \frac{q}{4\pi\kappa R_L} \tag{2}$$

where R_L is the fictious Laplace radius, which takes different geometries of nanoparticles (spheres, rods, discs, …) into account.

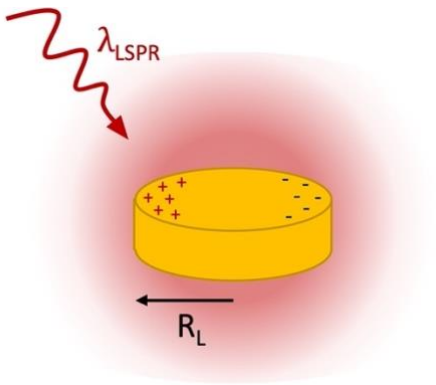

Figure 4. *Heat generation of a single plasmonic nanoparticle illuminated at its resonant wavelength* $\boldsymbol{\lambda_{LSPR}}$.

When several identical NPs are arranged in periodic arrays and illuminated at their resonance frequency (**Figure 5a**), the overall temperature increase not only arises from the sum of the individual contributions but it can also get enhanced by collective heating due to interactions between them.[29] Accordingly, the temperature increase ΔT_j induced by a NP j within an assembly of such, consists of a self-induced part ΔT_j^s and an external contribution ΔT_j^{ext} of the *N-1* surrounding particles:

$$\Delta T_j = \Delta T_j^s + \Delta T_j^{ext} \ . \tag{3}$$

The self-induced fraction ΔT_j^s can be calculated from equation 2, while ΔT_j^{ext} arises from the sum of the individually produced heat over all other particles at positions $\overrightarrow{r_k}$:

$$\Delta T_j^{ext} = \sum_{k=1,k\neq j}^{N} \frac{q}{4\pi\kappa} \frac{1}{|\vec{r_j} - \vec{r_k}|} \,. \tag{4}$$

Depending on the geometry of the array and the size of the nanoparticles, two particular temperature distributions throughout the array can be achieved: a *temperature confined regime*, where only the proximity of the NP is heated, or a *temperature delocalized regime* with a homogeneous temperature distribution. There, collective heating contributions become dominant, and a large volume occupied by the whole array is heated.

The degree of temperature confinement can be represented by a dimensionless confinement parameter ζ, which is based on the proportion of ΔT_j^s to ΔT_j^{ext}.
For 2D periodic arrays this proportion derives to:

$$\zeta = \frac{p^2}{3DR_L} \approx \frac{\Delta T_j^s}{\Delta T_j^{ext}} \,. \tag{5}$$

For $\zeta >> 1$ one obtains a temperature distribution, which is confined (**Figure 5b**), while it is delocalized for $\zeta << 1$ (**Figure 5c**). Therefore, to achieve uniform heating of the surrounding material, the featured parameters must be set in such a way that the external temperature contribution is exceeding the self-induced, leading to a confinement parameter ζ smaller than 1. Accordingly, it can be seen to that an arrangement leading to a confinement factor of $\zeta = 1.66$ shows local heat increase (**Figure 5b**) while the design with $\zeta = 0.18$ is resulting in an even temperature rise throughout the whole arrays (**Figure 5c**).[29]

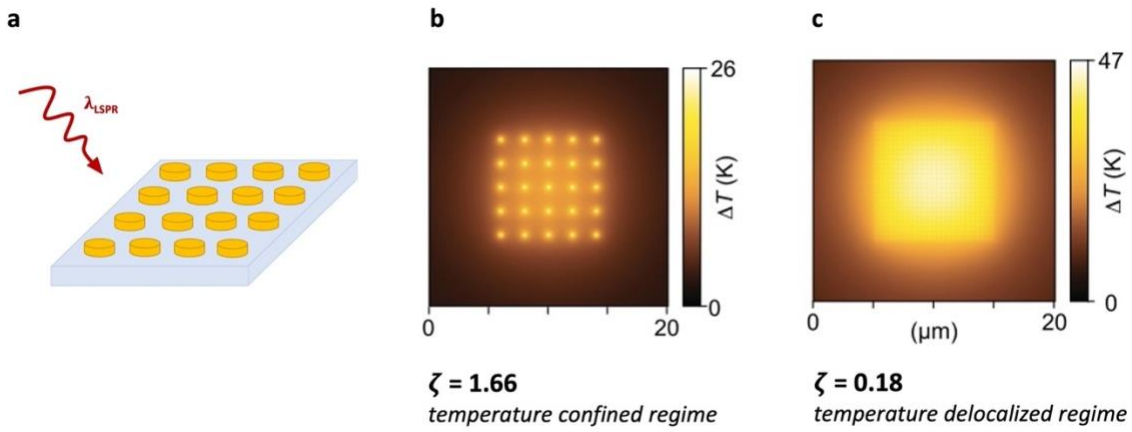

Figure 5. *a) sketch of the periodic nanoparticle array; b) numerical simulation of a temperature defined regime with ζ = 1.66; c) numerical simulation of a temperature delocalized regime with ζ = 0.18. [adapted from* [29]*]*

As described above, plasmonic heating allows heating *locally* by irradiation. Additionally, it was shown by Berto *et al.*[30], that it is also a very *rapid* and *reversible* process. They defined a characteristic time scale τ for a two-dimensional periodic NP array with $\zeta << 1$ (continuous regime) embedded in a surrounding medium to thermally respond to plasmonic irradiation:

$$\tau = \frac{D^2}{4a_s} \tag{6}$$

where D^2 is the illuminated area and a_s the thermal diffusivity of the NP environment.[30] Winkler *et al.* experimentally confirmed this prediction with measuring response times τ of tens of microseconds in a plasmonic system of a gold NP array surrounded by a water-polymer matrix that was irradiated on a circular footprint of ~ 20 μm^2. [24]
The rapid, reversible and local manner of plasmonic heating offers a wide range of applications in multiple biomedical fields, as e.g. in photo-thermal cancer therapy [31,32], biosensing [33] or drug delivery [34].

In various works, the kinetics of the phase transition between a swollen and a collapsed state of pNIPAAm architectures were investigated in a time-resolved manner. For example, it could be shown that the state transition of 30 nm thick pNIPAAm brushes induced by plasmonic heating occurs within 0.16 ms and follows a single-exponential trend.[24] In contrast, the study of 600 nm thick crosslinked networks of this polymer revealed more

complicated kinetics consisting of two consecutive phases: a first fast process of 100 ms attributed to fast water diffusion and a second, slower process requiring about 1 s, in which the outflow or the inflow of water is impeded by the denser architecture in the case of collapse, or by the rearrangement of the chains in the case of swelling. [26,35]

In this work, the phase transition that polymer networks of thermoresponsive pNIPAAm undergo under thermal stimulation is studied on the microsecond time scale by applying plasmonic heating. Furthermore, the impact of parameters influencing the transition, such as heating strength and duration as well as thermal preconditioning, will be observed to reveal the ultimate actuation speed and to show possibilities how such thermoresponsive pNIPAAm materials can be tailored in new applications.

2. Goals

Many biomedical and bioanalytical concepts as well as multiple applications in soft robotics use the phase transition of pNIPAAm for various tasks, for example in the form of sensitive capsules in drug delivery, as binding matrices in optical biosensors or as shape-morphing materials in biomimetic devices. Therefore, a detailed understanding of the collapse and swelling processes of pNIPAAm networks, as well as their response time to external thermal stimulation, is crucial to take developments a step further.

Previously, the kinetics of these transitions of macroscopic pNIPAAm networks were monitored on a time scale of minutes, depicting the correlation of gradually increasing temperature and refractive index changes associated to the change in thickness of such layer[26]. Furthermore, the temperature induced volume changes of surface tethered brushes of pNIPAAM were characterized by phase transition times even down to hundreds of microseconds[24]. Following on from this, this work is pursuing the investigation of the kinetics of the swelling and collapse of pNIPAAM networks upon rapid heating in the range of milliseconds under varying conditions (heating strength and duration, thermal preconditioning).

Therefore, a suitable substrate is fabricated, consisting of a thin layer of the polymer deposited onto an array of elliptical gold nanoparticles which are produced using UV laser lithography (UV-LIL). The morphology of the nanoparticle array is assessed by atomic force microscopy (AFM) and the thickness of the polymer layer is determined by surface plasmon resonance spectroscopy (SPRS). Fast temperature modulation is enabled by plasmonic heating realized by this gold particle arrays. In order to measure the phase transition of the gel, a dedicated optical system needs to be developed, which allows rapid optical heating and probing of the hydrogel layer simultaneously.
The methods of UV-LIL, hydrogel preparation, AFM and SPRS and a list of components are explained in Chapter 3. The experimental method, the substrate characterization, the

measurement calibration and the observations on the phase transition kinetics and its ultimate speed are comprised and discussed in Chapter 4. The thesis is completed with a conclusion and an outlook in Chapter 5.

3. Methods: Design of active plasmonic nanostructures

3.1 UV-laser interference lithography for metallic nanostructure fabrication

Gold nanoparticle arrays were produced with UV-laser interference lithography (UV-LIL). In this method an interference pattern, formed by coherent overlapping light beams, is recorded onto a thin photosensitive film, a photoresist. The interference field was generated by using an optical setup with Lloyd's Mirror configuration, see **Figure 6a**.

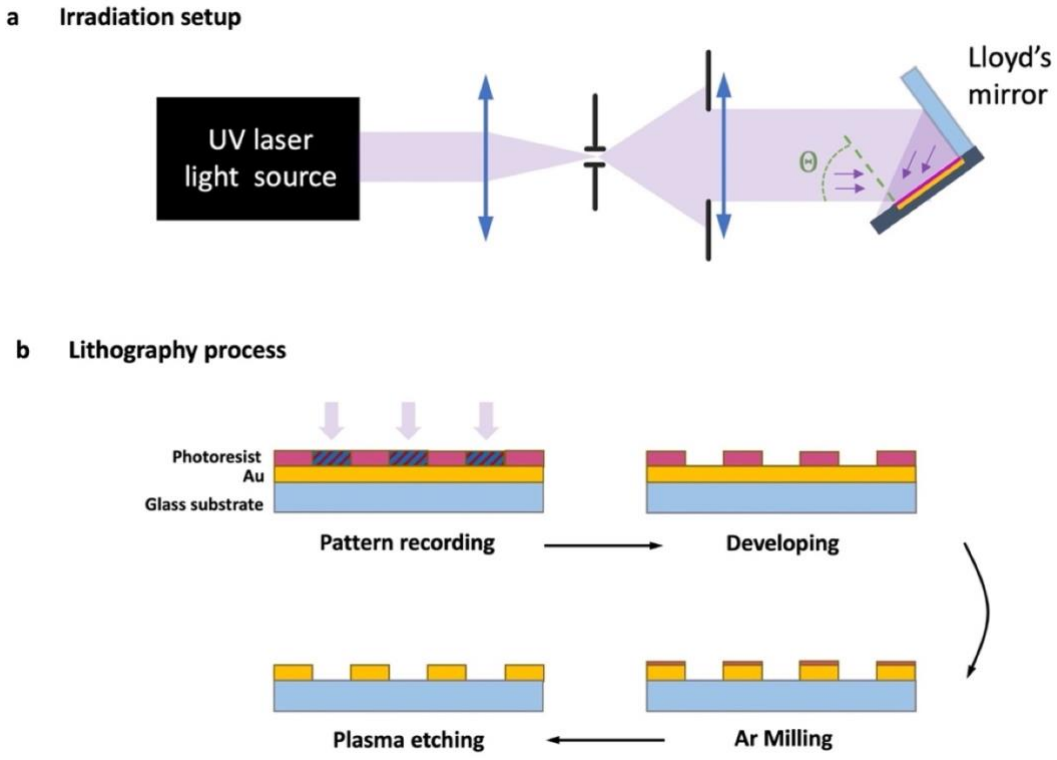

Figure 6. *a) Optical setup with Lloyd's Mirror configuration; b) four-step process of UV-LIL. [reproduced from [36]]*

By rotating the substrate by 90°, two orthogonally oriented grid-like intensity patterns are superimposed and produce a chessboard-like irradiation distribution. As can be followed in Figure 5b, after recording the interference pattern to a photoresist, the specimen is treated

with a developer solution, which is washing off the photosensitive layer that became soluble where it experienced sufficient high intensity irradiation. To transfer the recorded pattern onto the gold layer below the photoresist, argon milling is applied removing the metal in all areas which are not protected by the photoresist. Gold domains remain, arranged in a periodic array which is following the interference pattern recorded to the photoresist. In a final step, the residual resist is gently removed with ozone cleaning or plasma etching. The detailed protocol for the gold nanorod arrays manufacturing is described in the following:

Piranha cleaning

For a clean substrate basis, a BK7 glass slide was cut to dimensions of 25 x 25 mm and treated with acidic piranha solution. Therefore, the slide was immersed in a H_2SO_4 : H_2O_2 (3:1) solution for one hour and rinsed three times with water. After, it was sonicated consecuting in MiliQ, Hellmanex 1 % solution, MiliQ and finally Ethanol for 15 minutes each.

MPTMS deposition

As a transparent and non-conductive adhesive for a gold film a layer of (3-mercaptopropyl)trimethoxysilane (MPTMS) was deposited onto the glass slide, following the protocol of de la Chapelle et al..[37] Accordingly, the substrate was left in a solution of 2 ml MPTMS, 2 ml H_2O and 80 ml 2-propanol overnight (∼12h). The solution with the sample was brought to a boil (∼140°C) and simmered for 10 minutes. Then, the substrate was taken out, rinsed with 2-propanol, blow dried with an air gun, and cured on a hotplate at 110°C for 8 minutes. The boiling and curing process was repeated two more times.

Gold evaporation

To produce a layer, from which the particles can be milled, 50 nm of gold (MaTeck, cat. No. 900426) were deposited onto the substrate in a vacuum thermal evaporator (HHV Ltd, Auto306 Lab Coater) at a pressure below 10^{-6} bar and a deposition rate of 1-2 $\frac{\text{nm}}{\text{min}}$.

UV-Laser interference lithography

For the lithography process the gold chip was firstly spin-coated with a 100 nm thick layer of positive S1805 (1:2 diluted in PGMA) photoresist for 45 sec at 4500 rpm and cured for

2 min at 98°C. Then, the photosensitive substrate was irradiated by a coherent beam emitted from a He:Cd laser (IK 3031 R-C, λ = 325 nm, $I \approx 12$ $\frac{\mu W}{cm^2}$), which was expanded and collimated by a focusing lens, a pin hole and a collimating lens, before reflecting at the Lloyd's mirror creating interference. For obtaining an elliptically shaped particle geometry, the two irradiation times with the parallel and perpendicular orientation were set to 7 and 4 min respectively. In order to set a period Λ = 450 nm, the angle of the interfering beams θ was set to 21.17° to fulfill the relation $\Lambda = \frac{\lambda}{2 \sin\Theta}$ in correlation to Bragg's Law.

In the next step, the irradiated photoresist was washed off in a 1:17 developer solution of AZ-303 and deionized water for 4 min and 45 sec. To avoid inhomogeneities, the developer solution was stirred for half an hour at 1200 rpm in advance.

For the transfer of the photoresist structure onto the gold layer, the specimen was dry etched with accelerated argon ions (Roth & Rau IonSys 500, Germany, 5 x 2 min etching with 2 min pauses in between, acceleration energy of 500 eV). Finally, the remaining photoresist was removed by 20 minutes of ozone cleaning, resulting in a resist-free two-dimensional Au nanoparticle array.

3.2 Hydrogel deposition

A thin pNIPAAm-based film was deposited on the metallic nanostructure. For that, the substrate was firstly kept in a sealed container with a 1 mM benzophenone disulfide (4 AMBP-Disulfide) in dimethyl sulfoxide (DMSO) solution overnight. Next, it was rinsed with 100 % ethanol and dried under a nitrogen stream. For an approximately 100 nm thick polymer layer, a 2% pNIPAAm-based polymer dissolved in ethanol solution was prepared and spin-coated on the surface at room temperature (no ramp, 2000 rpm, 120 sec). The chemical structure of the pNIPAAm based polymer with photo-reactive benzophenone groups can be seen in **Figure 7**. Afterwards, the substrate was dried in a vacuum oven at 50°C for half a day to evaporate the remaining ethanol. Finally, the pNIPAAm layer was crosslinked in a UV box by irradiation dose of 2 $\frac{J}{cm^2}$ to generate a three-dimensional network.

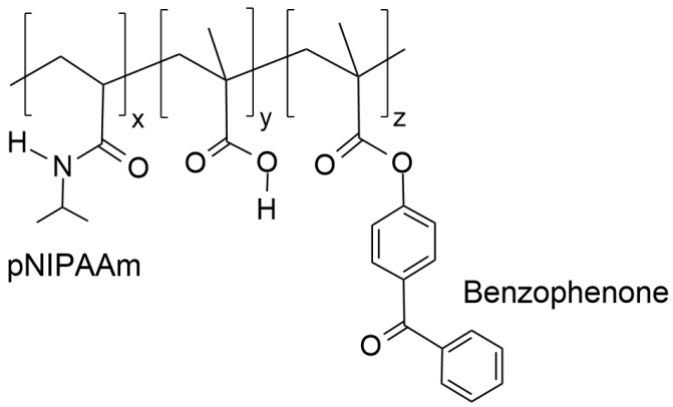

Figure 7. *Chemical structure of pNIPAAm polymer with photo-reactive benzophenone moiety. [adapted from [21]]*

3.3 Substrate Characterization

The morphology of the nanoparticle arrays was obtained with atomic force microscopy (AFM) and the thickness and swelling ratio of the hydrogel film were characterized by surface plasmon resonance spectroscopy (SPR). The underlaying methods are described in the following.

3.3.1 Morphology analysis with atomic force microscopy

The surface topography of nanostructures can be revealed and analysed with AFM by scanning molecular forces between the surface and a nanoscopic tip at a very short distance. It was developed 1986 by Binning, Quate and Gerber as a follow of a successor of the scanning tunnelling microscope (STM).[38] In contrast to the STM, atomic force microscopy allows three-dimensional nanoscopic to atomic scale imaging with high resolution not only for conductive, but for almost any material, such as metals, polymers, ceramics and even biological samples and furthermore does not require special sample preparation. [39]

As schematically shown in **Figure 8**, the crucial component in an AFM is a small tip attached to the end of a flexible cantilever, which is interacting with the surface atoms at close distance. These cantilever tips are etched from silicon (Si) or silicon nitride (Si_3N_4) to nanoscopic and even monoatomic sharpness. [40]

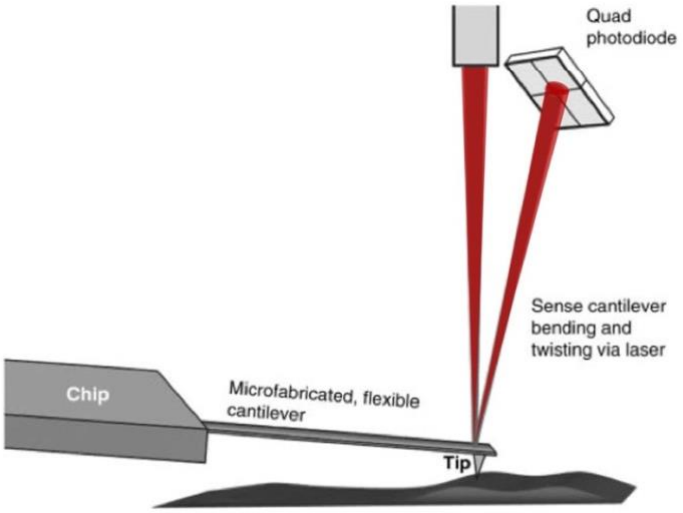

Figure 8. *Laser path with a reflecting cantilever holding the scanning tip and a photodiode in atomic force microscopy, adjusted from* [40].

While the tip scans the surface, the gap in between is varying according to the topography and thus the molecular interaction forces. Those either repulsive or attractive forces are bending the cantilever upwards or downward, respectively. The deflection of the cantilever is recognized by a segmented photodiode detecting the actuated reflection of a laser beam focused on the cantilever. [40,41]

The microscope can be operated in different modes. In the *static contact mode*, the tip is in direct mechanical contact with the surface (less than a few Angstroms). Due to the small distance between the interacting atoms, repulsive van der Waals forces are acting on the tip and the cantilever. The surface characteristic is either recorded by holding the height of the cantilever constant and measuring its deflection, or by adjusting the necessary height of the cantilever to keep the interaction forces constant.[39]

In the *dynamic non-contact* and *tapping modes*, the cantilever is let to resonantly oscillate. Changes in the surface distance shift the resonance frequency, which is either taken directly as a measured variable (non-contact mode) or indirectly by measuring and regulating amplitude and phase of the deviating frequency (tapping mode).

3.3.2 Layer thickness determination with surface plasmon resonance spectroscopy

The thickness of thin polymer layers can be determined by surface plasmon resonance spectroscopy (SPRS). There, the excitation of surface plasmons (SP) is used to detect

changes in the refractive index of the layer and thereby gain information about its dimensions.

Surface plasmons are optical waves that arise from electromagnetically exited oscillations of the electron density in a metal and propagate on its interface with an affiliated dielectric, see **Figure 9a**. [42]

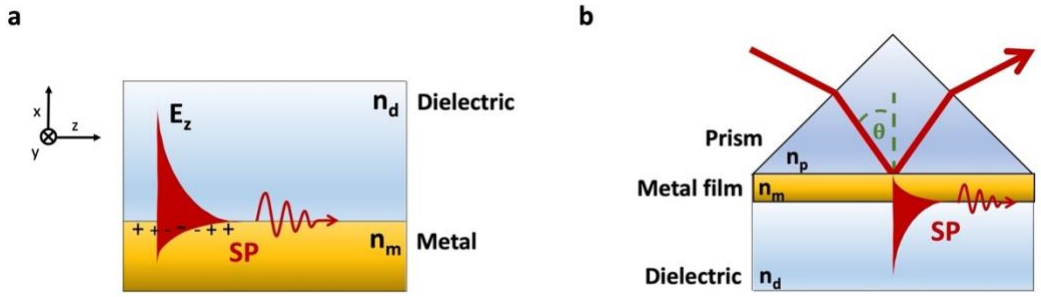

Figure 9. *a) Surface plasmons propagating on a metal-dielectric interface; b) Excitation of SP in Kretschmann configuration.*

Their propagation on the interface is described by a complex propagation constant β:

$$\beta = k_0 \sqrt{\frac{{n_m}^2 \ {n_d}^2}{{n_m}^2 + {n_d}^2}} \ , \tag{7}$$

where $k_0 = \frac{2\pi}{\lambda}$ denotes the wave vector in vacuum, λ the wavelength and n_m and n_d the refrective indices of the metal and the dielectric respectively. Most of the associated electric field extends perpendicularly to the interface up to several hundred nanometres into the dielectric layer with its magnitude decreasing exponentially.[43]

Optical excitation of surface plasmons

Surface plasmons can be excited by coupling light to a metallic surface via prisms [44,45] or by diffraction at the surface of metallic gratings [46]. Prism couplers – assembled either in *Otto* or in *Kretschmann* configuration - make use of the attenuated total reflection (ATR) of a light beam that is passing through a high refractive index prism. There, the beam is reflected at the base which is in contact with a medium of lower refractive index. In the

Kretschmann configuration, the prism base is positioned directly on top of a metallic film, that is in contact with the dielectric on its backside (Figure 7b). In case of total reflection at the prism base with incident angle θ, the light beam generates an evanescent field within the metal layer, which penetrates through the metal into the dielectric and excites the surface plasmons in the metal-dielectric interface when the matching condition is fulfilled:

$$k_0 n_p sin\theta = Re(\beta)\,, \tag{8}$$

The left-hand side of the equation describes the propagation of the incoming light beam components parallel to the surface, while the right-hand side equals the real part of the propagation constant of the surface plasmons. [47]

In optical measurements, the excitation of surface plasmons by electromagnetic radiation becomes visible as a characteristic resonant reflectivity minimum, the surface plasmon resonance (SPR). [47] According to the coupling condition given in **Equation 8**, changes in the refractive index, particularly that of the dielectric layer, lead to a shift of the SPR, which can be monitored in intensity spectra as a function of either the wavelength (spectrum of a white light source at a fixed angle of incidence), the angle of incidence (spectrum of a monochromatic light source at varying angles), or the detected intensity changes (at fixed wavelength and angle), see **Figure 10**. [48] As the refractive index of a medium is amongst others depending on the thickness of it, SPRS can be used to track/detect changes in the refractive index and can assign them to particular layer thicknesses of the involved media.[26,49]

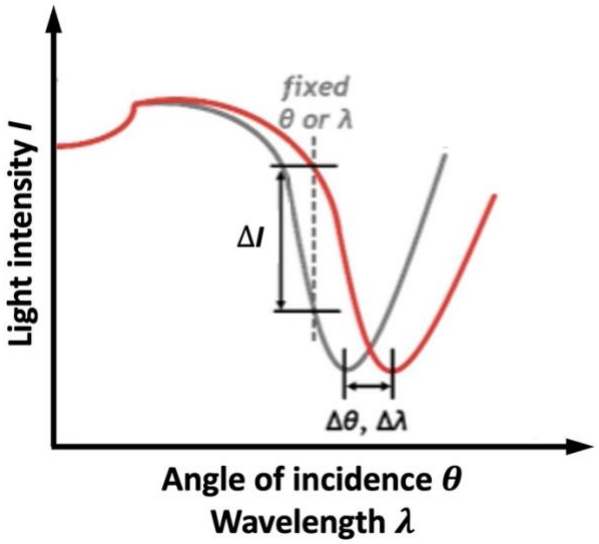

Figure 10. *SPR shift in wavelength and angle of incidence characteristic and associated change in intensity of reflected beam [adapted from* [50]*]*

4. Results

To investigate the transition of the pNIPAAm-based polymer network undergoing swelling and collapse, arrays of gold nanoparticles were introduced in the hydrogel structure. On the one hand, they serve to quickly heat the polymer network by using plasmonic heating, on the other hand, they are used to simultaneously observe the thereby thermally induced phase transition in the form of SPR shifts due to changes in the refractive index.

For this purpose, elliptically shaped nanoparticles were produced. Corresponding to the different lengths of the defining axes, the elliptical shape offers two distinct localized surface plasmon resonances (LSPRs), each of which can be excited by the corresponding polarization of an incident light beam (**Figure 11a**). In a developed optical system, one of these resonances is excited by a heating laser with a wavelength of λ_h = 785 nm to generate rapid plasmonic heating via Ohmic losses. Meanwhile the transmission of a monochromatic probing beam at λ_p = 633nm is monitored around the wavelength of the LSPR in order to observe changes in transmission due to the phase transition of pNIPAAm-based hydrogel related volume and refractive index changes (**Figure 11b**). The laser induced temperature increase is measured by connecting LSPR shifts originating from bulk heating to those induced by plasmonic heating.

Three experiments will be pursued to investigate the collapse and swelling transition of the polymer under specific conditions such as *local heating strength*, *changes in bulk ambient temperature* and *varying heating periods*.

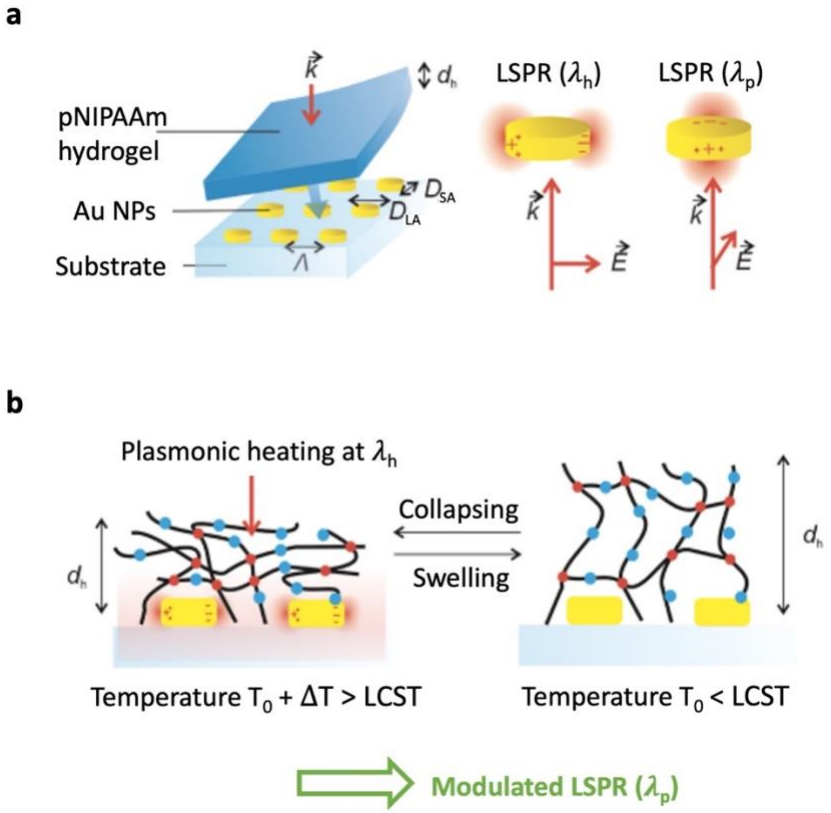

Figure 11. *Experimental concept: a) scheme of the substrate consisting of a pNIPAAm hydrogel layer, attached to arrays of elliptical nanoparticles with two distinct LSPRs; b) swelling and collapsing hydrogel structure resulting in shifts of the probing LSPR* $\boldsymbol{\lambda_p}$*. [adapted from [27]]*

4.1 Substrate characterisation

4.1.1 Properties of the nanoparticles NPs

Elliptically shaped nanoparticles were designed to support LSPR at the distinct wavelengths matching the heating and the probing laser. The LSPR can be shifted by adjusting the geometry of the particles in the UV-LIL fabrication process. The dimensions of the nanoparticles were measured with AFM, as presented in **Figure 12**. They show a long axis length of D_{LA} = (260 ± 20) nm, a short axis length of D_{SA} = (200 ± 10) nm and a height of h = 95 nm, however about 45 nm need to be subtracted due to the remaining photoresist, which was washed off afterwards.

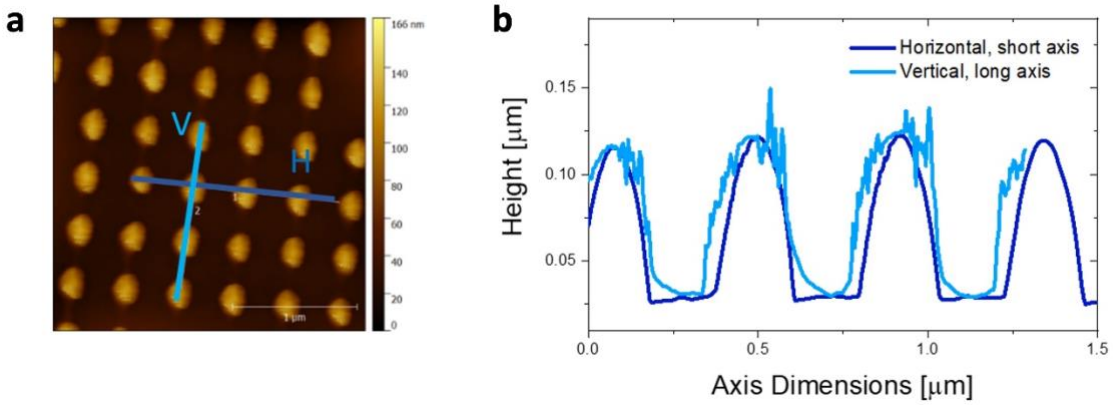

Figure 12. *a) (2.5 x 2.5) µm² picture of the nanorod distribution; b) Profiles of the nanorods marked in Figure 9 a, showing the dimension D_{LA} x D_{SA} x h = (260 x 200 x 95) µm³*

As the transmission spectra presented in **Figure 13** show, the long and the short axes correspond to resonances at λ_V = 867.9 nm and λ_H = 693.1 nm, respectively. Thereby, the vertically excited resonance λ_V allows to induce plasmonic heating with the laser of the wavelength λ_h = 785 nm, while the horizontal resonance λ_h is suitable for the probing of the structure with the second laser of λ_p = 633 nm.

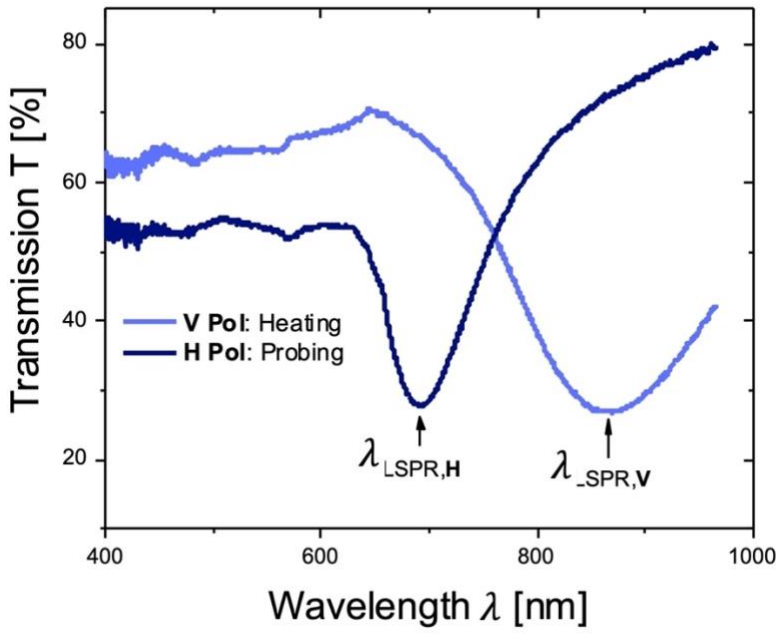

Figure 13. *Wavelength transmission measurement of the bare nanoparticle arrays immersed in water for vertical and horizontal white light polarization and resulting LSPRs* $\boldsymbol{\lambda_H}$ *and* $\boldsymbol{\lambda_V}$.

4.1.2 Properties of the hydrogel film

The hydrogel film was characterized using surface plasmon resonance spectroscopy in Kretschmann configuration. Therefore, reflectivity spectra R(θ) of the pNIPAAM film deposited on a flat gold layer (approaching the surface with gold elliptical nanoparticles) were recorded in dry and in water-swollen state at room temperature T = 24 °C. More precisely, the transverse magnetic (TM mode) and electric modes (TE mode) of a monochromatic beam that was reflected at the gold-prism interface were recorded as a function of the angle of incidence θ. The spectra were fitted with the Fresnel reflecting model implemented in the software *Winspall* as can be followed in **Figure 14**, and the thicknesses of the gold and polymer layers could be derived from the parameters of the fit.

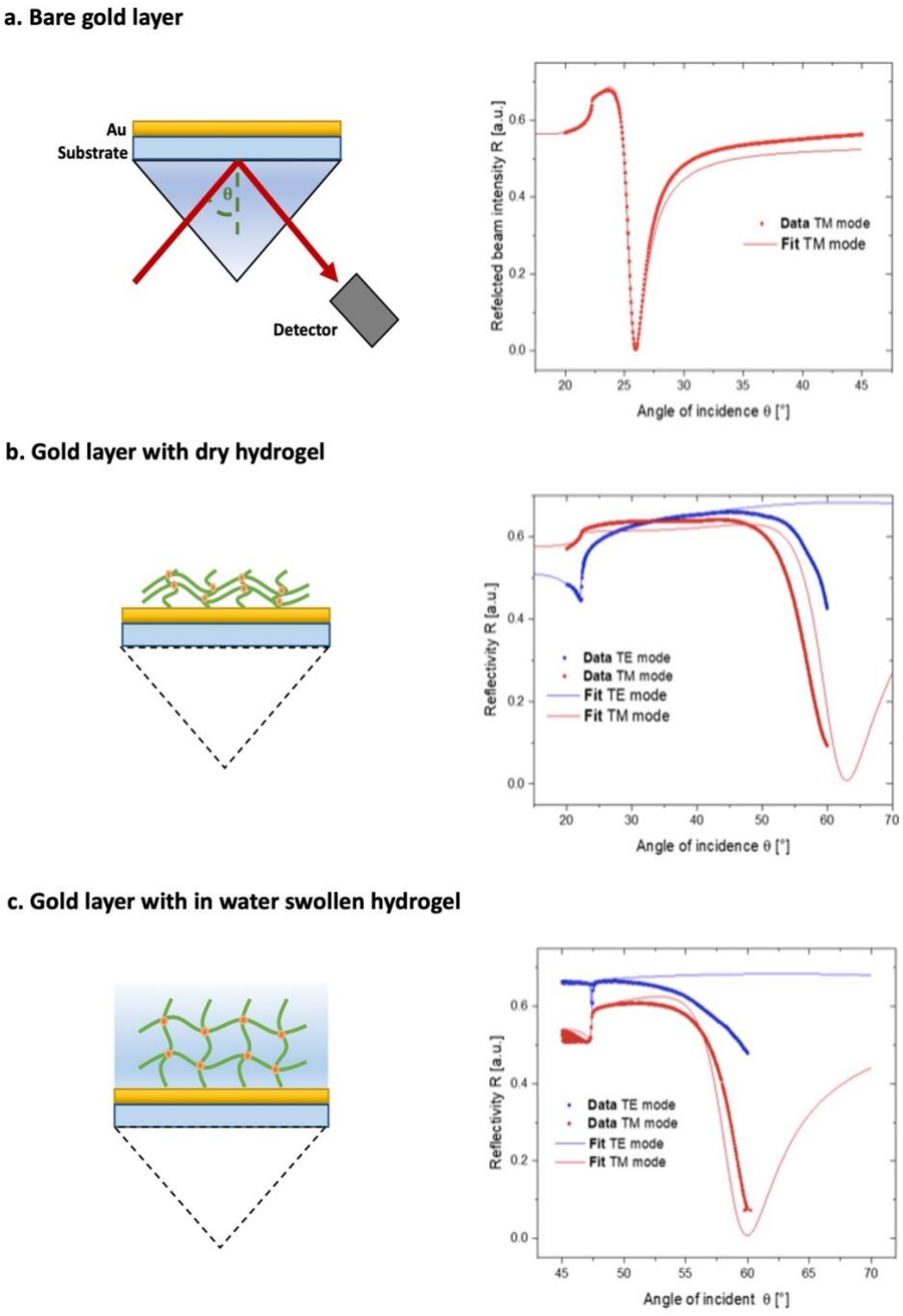

Figure 14. *Sketches of the various layer compositions and set-up configuration on the left and associated SPR-measured reflectivity spectra and fits on the right of a. bare gold as a reference; b. gold with deposited dry hydrogel layer; and c. gold with a swollen hydrogel atop*

Consequently, these measurements revealed a thickness for the gold film of d_{Au} = 48.82 nm and a thickness of d_h = 104 nm with an associated refractive index of n_h = 1.48 for the dry pNIPAAm film. Swollen in water the pNIPAAm polymer film expanded to a thickness of d_h = 843 nm with a refractive index of n_h = 1.35. Additionally, when the temperature is increased above the LCST to T = 40 °C, the hydrogel collapses to a height of with d_h = 180

nm with a refractive index of n_h = 1.42.[21] The properties of the hydrogel layer are summarized in **Table 1**.

	Thickness d_h [nm]	*Refractive index n_h*
Dry hydrogel	104	1.48
Swollen hydrogel (T = 24 °C)	843	1.35
Swollen hydrogel (T = 40°C) [21]	180	1.42

Table 1. *Summarized layer thicknesses* d_h *and refractive indices* n_h *under different conditions*

4.2 Optical system

To measure the phase transition of the polymer network with high time-resolution, an optical system was built, for simultaneous heating and probing of the polymer structure. Fundamental to this heating and probing method is that the investigated substrate carries elliptical nanoparticles with two LSPRs, each of which is excited by vertically and horizontally polarized light. The optical observation system itself is based on a polychromatic white light source and two monochromatic laser beams for both resonances dedicated to one of the resonances each. While a high-power heating laser is exciting the vertical resonance to induce plasmonic heating, a second laser, the probing beam, is used for tracking the transmission changes at the wavelength corresponding to the steepest slope of the horizontally excited resonance. At this position, the change of transmission will be the most significant when the structure is collapsing or swelling. The altered probing beam intensity is tracked by a photodiode and an oscilloscope, see **Figure 15**.

To maximize the signal-to-noise ratio both laser beams need to be strongly focused and aligned on the surface of the substrate. With this aim, a microscope was implemented, which in combination with the white light source also allowed to navigate on the substrate and record white light transmission spectra. The white light source was also employed to record transmission spectra of the substrate. The set-up of the measurement system is explained in the following in detail and can be retraced in the scheme in **Figure 16**.

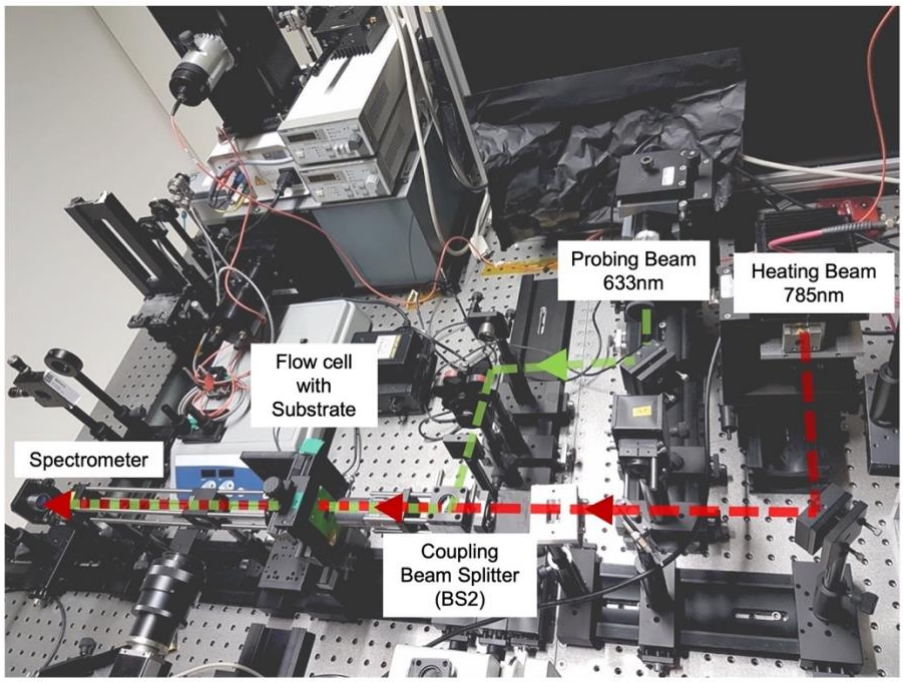

Figure 15. *Picture of the developed measurement device and outlined main beam paths*

4.2.1 Optical set-up

The scheme of the optical system is shown in **Figure 16**. As can be seen, the λ_h = 785 nm heating and a λ_p = 633 nm probing beam are coupled in a beam splitter (BS2) before being focused by a microscope objective (L2) onto the surface of the substrate. It is mounted in a home-built flow-cell, which is connected to a pump for transporting liquid samples and a temperature controller with a Peltier element. After passing through the substrate clamped in the flow-cell, the overlaying beams are re-collimated by a second microscope objective (L3) and either get redirected towards a CCD camera for monitoring focusing and beam alignment, or the beams are allowed to travel to a spectrometer or photodiode. Here, they are passing a Notch filter (LNF) in order to block the high energy heating beam. The intensity of the probing laser beam is then recorded in a photodiode (PD2) connected to an oscilloscope.

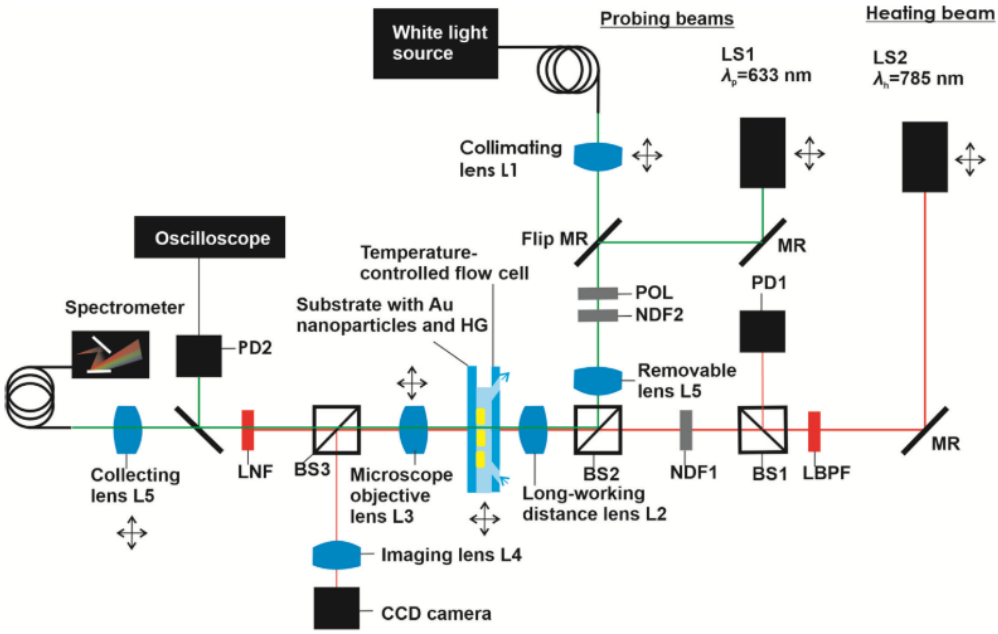

Figure 16. *Detailed scheme of the developed optical system. reproduced from* [27]*]*

By flipping a mirror (Flip MR) in the beginning of the probing beam's path, the light source can be switched to a collimated white light source. By directing the polychromatic probing beam path to a spectrometer instead of the photodiode in the end, transmission wavelength spectra can be recorded. Furthermore, by implementing a defocussing lens (L5) ahead of the BS2, the polychromatic beam is made irradiating a large area on the sensor surface that is imaged to the CCD, which is creating a microscope.

Staying permanently the heating laser is passing a bandpass (LBPF) and a neutral density filter (NDF1). A small part of the signal, diverted in a beam splitter (BS1), is used to monitor the intensity of the heating laser with another photodiode (PD1) which is also connected to the oscilloscope.

4.2.2 List of optical components

As light sources the TOPTICA PHOTONICS iBeams smart ws wavelength stabilized Diode Laser 785 nm, 250 mW (Germany) and the Melles Griot stabilized HeNe Laser system 633 nm (USA) were used to generate the heating and probing beams. The white light was originating from a 12 V halogen lamp (LSH102 LOT-Oriel, Germany). The Mitutoyo MPlan Apo 50x/0.55 ∞/0 f = 200 (Japan) was employed for the focusing microscope objective L2 and the Olympus MPlan 10x/0.25 ∞/– (Japan) served as the

collecting objective (L3). The beam splitters in this system had splitting rates of 90:10 (BS1), 50:50 (BS2) and again 90:10 (BS3) and were purchased from THORLABS (US). For signal recording the Agilent Technologies DSO 1004A 60MHz 2GSa/s (United States) Oscilloscope and the Andor Technology, Shamrock 303 Spectrometer (Northern Ireland) were utilized. The temperature in the flow cell was controlled by the Wavelength Electronics, 5Amp-40Watt Temperature Controller, Model LFI-3751 (United States) and the flow rate kept regulated by the ISMATEC IPC, High Precision Multi-Channel Pump (Germany). The intensity of the light beams was measured with the portable Newport, Model 2936-R (United States) power meter. The signals in the spectrometer were processed with the Andor Solis software and later, as well as the data generated by the oscilloscope fitted and analysed in OriginPro 2018.

4.3 Static observation of swelling and collapse

Furthermore, measurements of wavelength transmission spectra were carried out with both polarizations, before and after the combined hydrogel nanoparticle system was heated and brought to collapse with a heating beam intensity I_h = 8 mW. Shown in **Figure 17**, the associated shift in resonance led to an increase in transmission of ΔT = 9.7% at the wavelength of λ_p = 633 nm that is coincident with the steep slope of the short wavelength LSPR dip. This change will be utilized in the later measurement as an increase in the intensity of the probing beam recorded by the photodiode and oscilloscope, enabling the measurement of the kinetics.

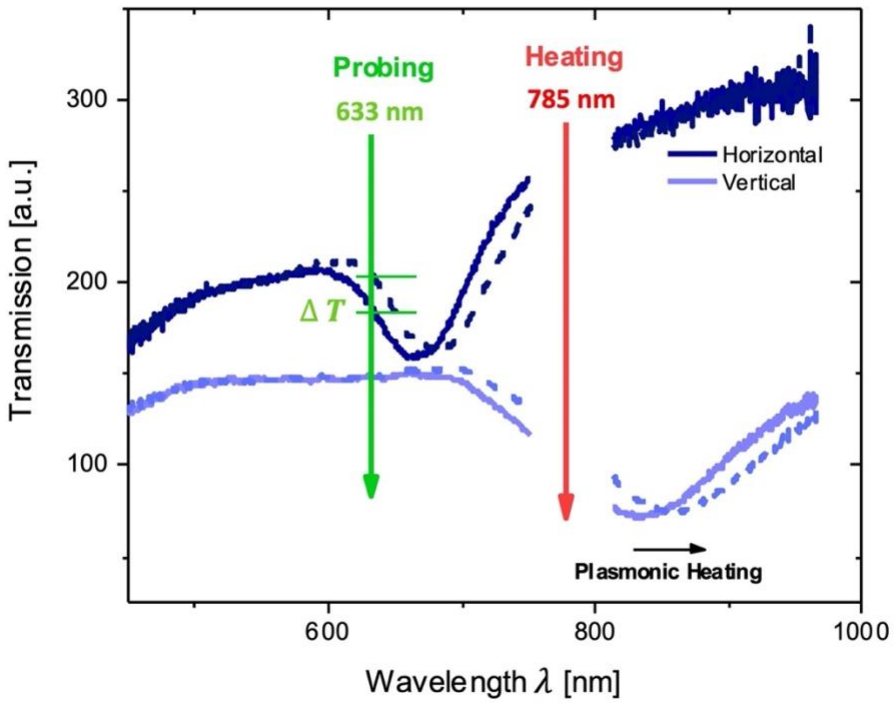

Figure 17. *Wavelength transmission spectra measurement of pNIPAAM in swollen (solid lines) and collapsed state (dashed lines), for horizontally and vertically polarized white light (dark and light blue). After the collapse, the LSPRs are shifting for both polarizations and the transmission is increasing about ΔT= 9.7% at the probing wavelength λ_p = 633 nm.*

4.4 Calibration of the plasmonic heating method

The actual temperature increase from laser-induced plasmonic heating is found by relating the LSPR-shifts generated by the heating beam λ_h with those measured for temperature controlled by a Peltier device on the whole sensor chip.

For this, the shift of the LSPR is observed during stepwise heating once with bulk heating and secondly with local laser irradiation at λ_h. Matching the two LSPR shifts, a thermometer can be created which is connecting temperature increase with applied laser power at λ_h. The measurements are presented in the following.

4.4.1 Bulk heating

Wavelength transmission measurements were recorded at different temperatures controlled by a Peltier element to track the LSPR shift, as shown in **Figure 18a**.

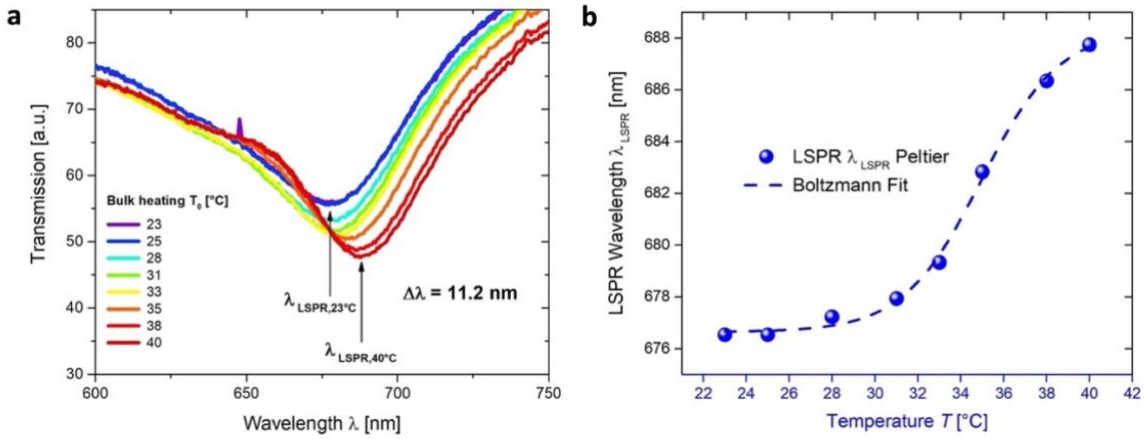

Figure 18. *Temperature dependent shift of the LSPR in a) transmission spectra; and in b) as a function of LSPR wavelength depending on temperature.*

The temperature was gradually increased from 23 °C to 40 °C resulting in a red-shift of the LSPR wavelength λ_{LSPR} due to the increased refractive index accompanying the temperature-induced collapse of the structure. The resonance went from $\lambda_{LSPR,23°C}$ = 676.5 nm to $\lambda_{LSPR,40°C}$ = 687.7 nm and thereby leading to a total difference of $\Delta\lambda$ = 11.2 nm. Plotting the LSPR wavelength shift against the associated temperatures gives a sigmoid curve typical for pNIPAAM represented in **Figure 18b**. With rising temperature, the resonance consistently shifts to longer wavelengths with a maximum change occurring around the LCST until it is flattening towards a constant value when above the LCST. The position of the steepest slope lays at 34°C and is thereby 2°C off the reported LCST of pNIPAAM of 32°C, which could be attributed to the construction of the flow cell and the temperature controller, where the temperature is measured on the upper surface of the flow cell. This gradient indicates the most significant section in the phase transition from the swollen to the collapsed state. Cooling the polymer matrix back to 23°C the LSPR shifts back to its original position which implies that the process is reversible.

4.4.2 Local plasmonic heating

The experiment is repeated, but instead of the bulk heating the underlaying gold nanoparticles are made acting as plasmonic nano heat sources to locally increase the temperature. The thereby induced shift of the resonance wavelength can be followed in **Figure 19a**.

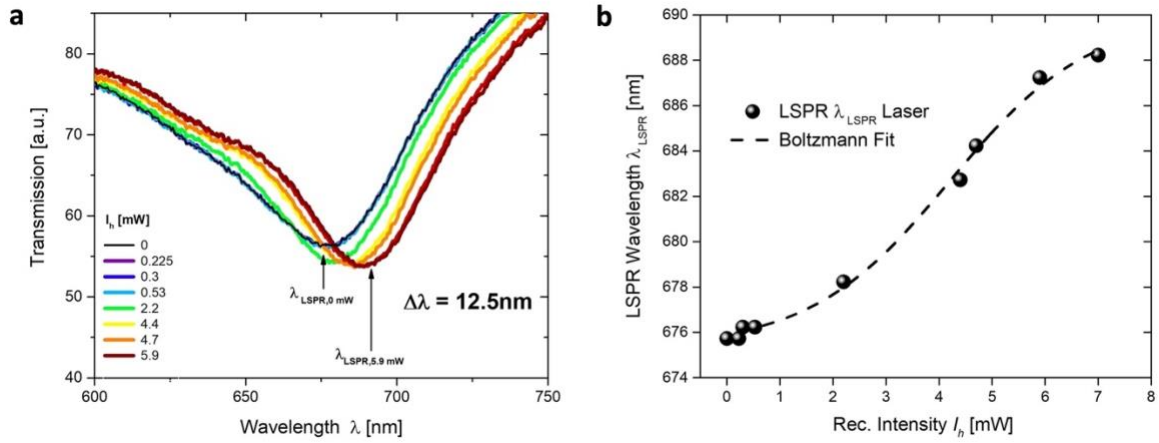

Figure 19. *Laser power dependent shift of the LSPR in a) transmission spectra; and in b) as a function of LSPR wavelength depending on the laser power.*

By step wise raising the intensity of heating laser from 0 to 5.9 mW (per an area with 30 µm diameter) a shift of $\Delta\lambda$ = 12.5 nm could be detected. With gradually increasing the heating laser intensity, the LSPR minimum is shifted from 676.5 nm up to 687.9 nm but is deviating from the theoretical sigmoid trend: over the main middle section, the dependence of the LSPR shifts on laser intensity exhibit a different profile compared to that measured for bulk temperature changes (**Figure 19b**). This deviation could be ascribed to the Gaussian profile of the heating beam intensity resulting in a gradient in the local temperature increase ΔT.

Nevertheless, a shift comparable to the one reached by conventional heating, could be generated, which indicates that plasmonic heating is a sufficient way of heating the pNIPAAM film.

In both measurements (**Figures 18a** and **19a**) one can observe a general drop in the transmission with increasing temperature or laser power respectively. It could be addressed to refractive index changes in the bulk medium due to the heating, which is therefore affecting more the first measurement with bulk heating than the second one where it only was only heated locally.

4.4.3 Calibration of refractive index changes

The two heating methods were compared to verify their compatibility and to establish a translation between applied heating laser power and actual temperature increase of the hydrogel layer. Both measurements exhibit the typical phase transition development of pNIPAAM, even though with plasmonic heating it was not following the theoretical sigmoid trend as pronounced as with conventional heating.

Connecting the two measurements via the LSPR wavelengths, a thermometer, showing which applied laser powers correlate to certain temperature changes, can be created, as can be seen in **Figure 20**. The fact that this relationship has close to linear character is backing up the hypothesis that plasmonic heating is heating the polymer structure in a comparable way as with Peltier heating.

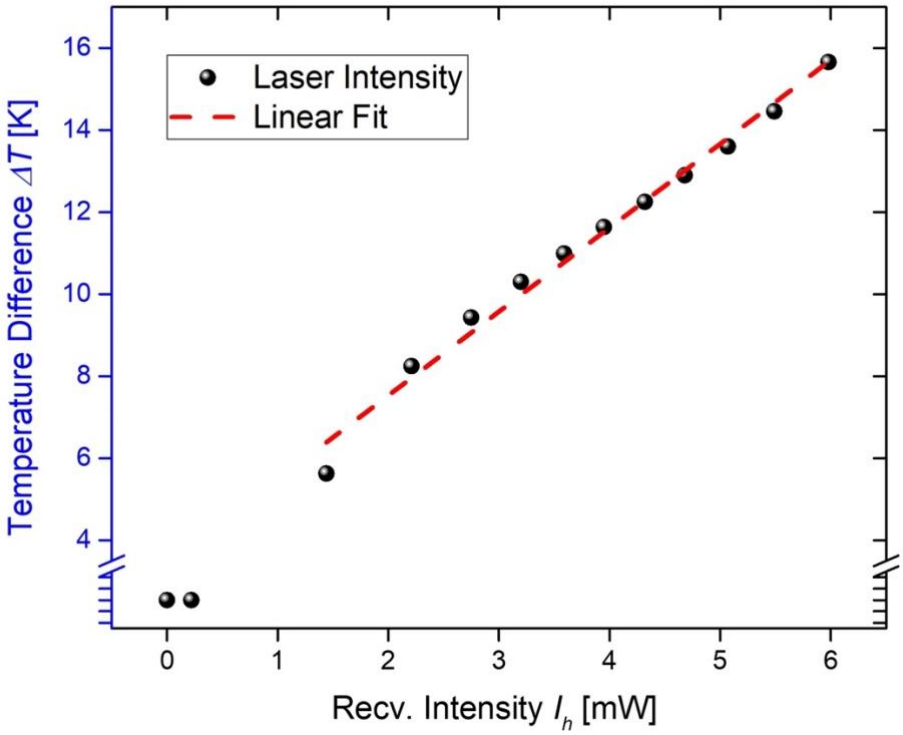

Figure 20. *Correlation between applied laser Intensities I and corresponding temperature Increase* ΔT.

4.5 Kinetics of the hydrogel phase transition

The optical system was set to the configuration, where the oscilloscope is recording intensity changes of the probing beam upon temperature increase. The substrate with nanoparticles, covered by the hydrogel layer, was irradiated by a series of short heating beam pulses. During the irradiation, the network heats up and collapses, resulting in an increase of received intensity due to changes in the refractive index. As soon as the heating laser beam is switched off, the system is cooling down and the pNIPAAm-based hydrogel relaxes back to its original swollen state, which is visible in a decrease of captured intensity. The temperature responds faster than a millisecond to the applied laser irradiation, which can be seen in **Figures 21** and **22** from the rapid drop in intensity immediately after the laser is turned on and the increase directly after it is turned off. This behaviour is opposite to that of the hydrogel structure and can be attributed to temperature-related changes in the refractive index of the water alone.

The phase transition kinetics of the pNIPAAm-network were observed in the following three experiments for different conditions: controlled local heating strength, changes in bulk ambient temperature and varying duration of the heating pulses. For that, the time constants τ of the swelling and collapsing process were determined in each case to describe the transition

4.5.1 Faster and more emphasized collapse with increased heating beam intensity

In the first experiment, the substrate was thermally preconditioned to an ambient temperature of T_0 = 25 °C and irradiated with t_h = 20 ms pulses of stepwise increasing heating laser powers I_h that resulted in temperature increases from ΔT = 3 to 15 K. Thereby, the collapse of the structure was induced during the irradiation by the heating laser and accompanied by an increase of intensity of the probing beam I_p. Subsequently, the structure was swelling back to its original state when the heating beam was switched off (I_p = 0). The pulsing was set to a frequency of ν = 10 Hz, allowing the network to come back to its original state in between the actuating pulses.

In **Figure 21a**, the intensity of the probing beam I_p received by the oscilloscope is shown for the swelling and the collapsing of the hydrogel film. The signals were fitted

exponentially, and the time constants τ_C and τ_{Sw} for the processes each were extracted and presented in **Figure 21b**.

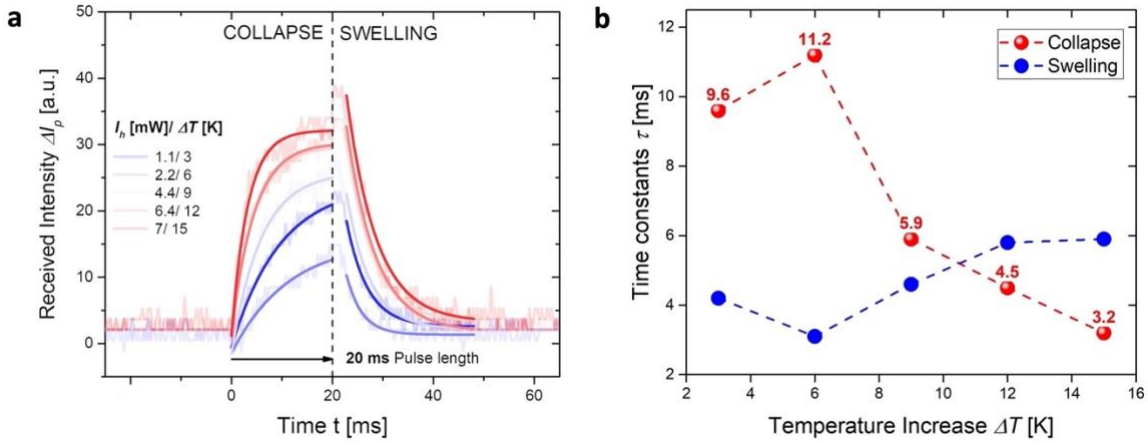

Figure 21. *a) Intensity changes due to collapsing and swelling of the pNIPAAM polymer network after 20 ms pulses of increasing laser power; and b) associated time constants.*

As can be seen, the higher the energy introduced into the system by I_h, the more I_p increases, which reflects the progressive state of polymer collapse. Furthermore, the decrease in the time constant τ_C from 9.6 to 3.2 ms for increasing ΔT from 3 to 15 K shows that the collapse process accelerates with increasing heating intensity.

As the increased temperature applied loosens hydrogen-bonds in the polymer, its hydrophobicity is increased and the water clusters hold by the polymer-water hydrate shells are destabilized. Consequently, the structure shrinks along with expelling of the water from the network. The higher is the temeprature, the more bonds are loosened, allowing more clusters to break while also boosting hydrophobicity and thereby speeding up the process of the collapse.

Once the laser was switched off, the polymer structure swelled back into its original state, visible in the associated drop of the kinetics back to the baseline. In contrast to the collapse, the swelling time constants τ_{Sw} stay in a closer range between approx. 4 and 6 ms, weakly changing with the temperature increase applied before.

4.5.2 Behaviour at different stages of pre-collapse by thermal preconditioning

In the second experiment, the ambient bulk temperature T_0 was set from 25 to 32 °C, visible in the elevated baseline in **Figure 22a**, followed by the heating pulse. The network collapse was triggered by pulses of t_h = 20 ms at ν = 10 Hz with full laser power I_h of 7 mW. The intensity was then measured for the different preheating conditions (**Figure 22a**) and time constants read out respectively (**Figure 22b**).

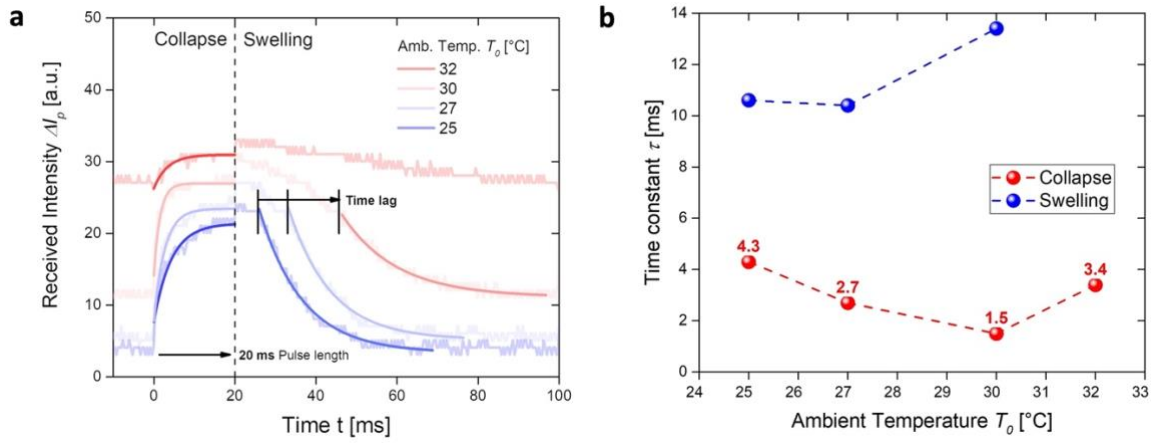

Figure 22. *a) Intensity changes of collapsing and swelling with increasing ambient bulk temperature; and b. associated time constants* $\boldsymbol{\tau_C}$ *and* $\boldsymbol{\tau_{Sw}}$

Approaching the LCST by preconditioning the bulk medium from 25 to 30 °C resulted in faster collapsing of the network which is visible in the decreasing time constants τ_C from 4.3 to 1.5 ms. As the network is already pre-collapsed (visible in the lifted baseline) only a small energy is necessary to complete the phase transition.

Interestingly, it was observed that after switching off the heating laser the swelling occurred in two phases. At the beginning the network changes slowly, and after a delay, the process progresses exponentially with time constants τ_{Sw} from 10.4 to 13.4 ms. These two distinct phases are more pronounced and elongated when T_0 approaches the LCST.

4.5.3 Full collapse in two steps during extended heating periods

Finally, the transition was studied for increasing heating periods. Therefore, the bulk temperature was set to T_0 = 23 °C and the substrate was treated with maximum laser power induced heating I_h = 7 mW, leading to a temperature increase of ΔT = 15 K for pulse lengths t_h from 10 to 60 ms. While the collapse could be fitted single-exponentially for heating periods up to 20 ms, the mono-exponential fitting was not meeting the data anymore for pulses longer longer than 60 ms (**Figure 23a**). Instead, a double exponential fit with two time constants $\tau_{C,1}$ and $\tau_{C,2}$ is more suitable, which is indicating that a second process is involved in the transition (see **Figure 23b**). In this way, the first part of the transition is characterized by a short time constant of $\tau_{C,1}$ = 1. 6 ms, along with a second step with the time constant $\tau_{C,2}$ = 23 ms.

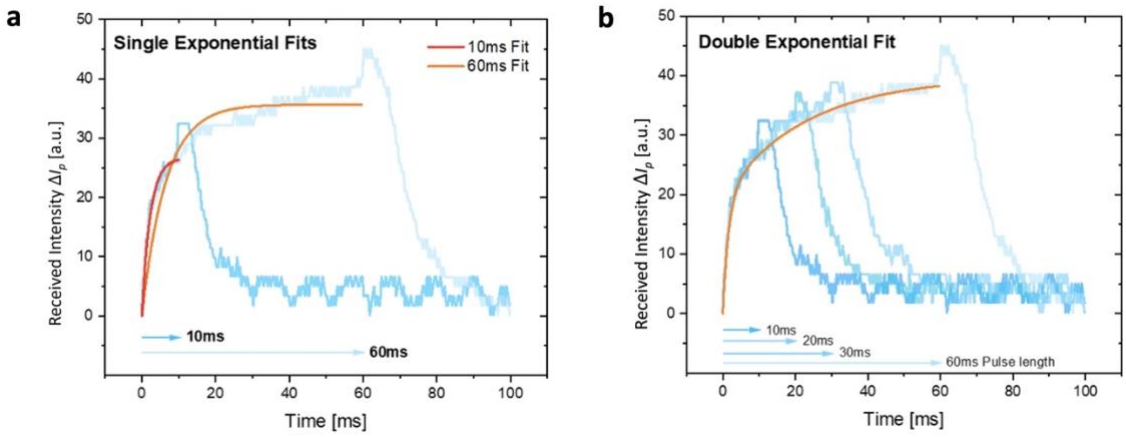

Figure 23. *a) Intensity changes of the collapse fitted with a single exponential fit; and b) double exponentially fitted*

The kinetics of the swelling on the other hand could be fitted single exponentially, independent from the before applied heating pulse duration, as can be seen in **Figure 24a**. Nevertheless, the process seems to consume more time after increased heating period as the process of collapsing progressed further, respectively. Consequently, this is shown by the increasing time constants from 3.9 to 8.0 ms for 10 and 60 ms long irradiation.

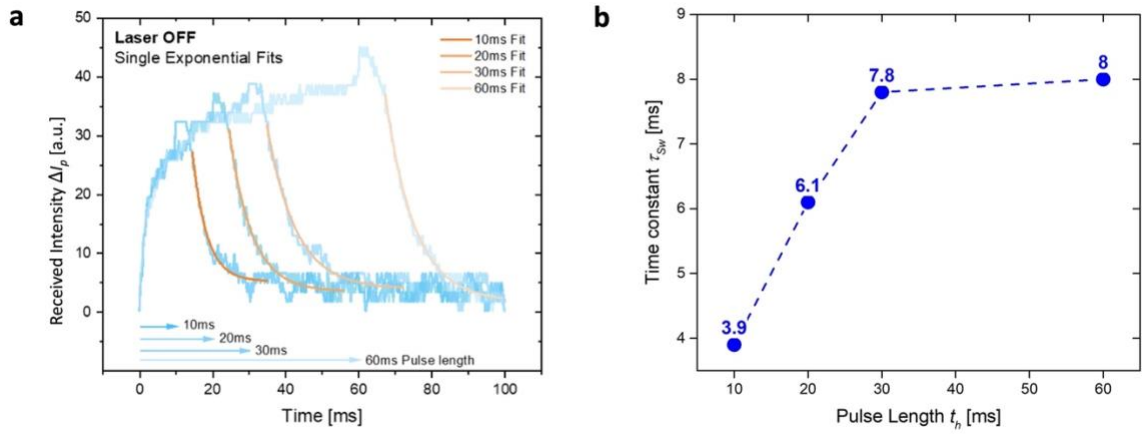

Figure 24 *a) Intensity changes due to the swelling after increasing heating duration; and b) associated time constants* τ_{Sw}.

In theory, the swelling and collapsing of such responsive polymer networks can be explained with models for the collective diffusion behaviour of their polymer chains [51–53]. There, a change in the volume of a polymer network layer, which can only expand perpendicularly to the surface, is represented by a displacement distance *u(x,t)*. Changes in the displacement distance can then be described by a Diffusion Equation, with *D* as the collective diffusion coefficient:

$$\frac{\partial u(x,t)}{\partial t} = \frac{\partial}{\partial t}\left(D\frac{\partial u(x,t)}{\partial x}\right). \tag{9}$$

With the Flory-like mean-field mixing energy and the osmotic bulk modulus $K = \phi\frac{\partial \Pi}{\partial \phi}$ [52], containing the polymer-volume fraction Φ and the osmotic pressure Π, one can express the diffusion coefficient *D* explicitly, which shows its dependency on the diffusion on the Flory-Huggins parameter χ [27,53] next to the constants *A*, *B*, *B'*:

$$\boldsymbol{D = A + B\chi\Phi(x,t)^2 = A - \frac{B'}{\left(1 + \frac{\partial u(x,t)}{\partial x}\right)^2}}. \tag{10}$$

The Flory-Huggins parameter χ indicates the miscibility of polymers in solvents and for thermoresponsive hydrogel in water, χ is temperature dependent [54]. Thus, the temperature can determine whether a solvent is a good solvent (lower χ) or a bad one (higher χ), either hindering or promoting the diffusion and thus affecting the phase transition. Following this,

a greater temperature stimulus ΔT as applied in the first experiment (**Figure 19a**) could increase the diffusion rate of the water out of the network and therefore accelerate the collapse.
Furthermore, following **Equation (10)** the diffusion *D* depends also on the distance to the surface *x* and the polymer volume fraction Φ, which is defined as:

$$\Phi = \frac{\Phi_0}{1 + \frac{\partial u}{\partial x}}\ , \tag{11}$$

with Φ_0 being the polymer volume fraction in the equilibrium state. This could explain why the swelling, contrary to the collapse, occurs with a time delay at increased ambient temperature in the second experiment (**Figure 22a**): If the diffusion is dependent on the polymer volume fraction Φ, the diffusion effectively decreases in areas with a high polymer density (Φ close to 1) and would slow down a phase transition there. Since the collapse starts from a swollen network and thus low Φ and high diffusion, the process can happen fast and exponential. Swelling, on the other hand, starts from a compact, collapsed state with high polymer density (high Φ) and thus low diffusion coefficient.
Simulations [27] suggested, that if D is dependent on χ that the swelling propagation slows down from the outside of the layer towards the inside close to the surface and is therefore a function of *x*. This would also delay the swelling at the inner interface.

Considering the hydrophilic-hydrophobic interactions between the polymer network and the water the faster network collapse due to the increased heating strength in the first experiment (**Figure 21**) could also be explained by the increased amount of broken hydrogen-bonds. As the applied energy loosens hydrogen-bonds in the polymer, its hydrophobicity increases and the water clusters hold by the polymer-water hydrate shells are destabilized, enabling faster diffusion [18]. Consequently, the structure shrinks along with expel of the water. The more energy is loaded into the system the more bonds are loosened, allowing more clusters to break while also boosting hydrophobicity and thereby speeding up the process of the collapse.

Also, the accelerated collapsing kinetic in a preconditioned environment in the second experiment (**Figure 22**) could be traced back to the open hydrogen-bonds and increased

hydrophobicity. As the network is already pre-collapsed (visible in the lifted baseline), many hydrogen bonds already broke and only a small energy is necessary to hit off the break-down of the hydrate shells, releasing the water clusters. Exceeding the LCST most of the phase transition seems to already have taken place, probably the change is more due to the diffusing water clusters then to the hydrophobic transition of the polymer.
This could eventually also explain the two phases observed for the swelling at varying temperature preconditioning. At higher ambient temperatures more hydrogen bonds are open and even though the structure itself is starting to unravel, leaning towards a more hydrophilic state, the water clusters are not stabilized yet and it takes longer until the network is back in equilibrium.

Finally, the reason for the two-step process for longer heating periods in the third experiment (**Figure 23**) could be, that the collective conformational change of the polymers might happen within the first 20 ms, the bonds stay open, and the water diffuses over a certain time. If one compares the transmission magnitude for 10 ms with the one of 60 ms one can see an extension of 40 %. This could indicate that, for short irradiation times (10 – 30 ms), the main process in the phase transition is the breaking of the hydrogel-bonds and only some shares of the water are expelled, whereas at longer irradiation times (60 ms) the network reaches strain relaxation, and the gel has more time for the water to diffuse.

5. Conclusion

The presented work shows that the swelling and collapse kinetics of thermoresponsive networks can be influenced by external parameters such as the applied heating strength, the temperature difference between the LCST and the ambient temperature and the heating pulse duration. For this purpose, a thin pNIPAAm-based hydrogel layer of about 800 nm thickness (in the swollen state) was attached on gold nanoparticle arrays to enable rapid plasmonic heating and simultaneous observation of induced phase transitions in a self-developed optical system.

It was possible to reveal that the response time of the network to rapid temperature changes is different for the collapse and swelling process. The collapse can be accelerated by increasing the heating strength, or by preconditioning the temperature of the surrounding medium closer to the LCST. These measures made it possible to achieve characteristic times of 3.2 and even 1.5 ms. With longer heating duration, another superimposed transition process with a time constant of > 20 ms was found, which was not observed before in similar experiments with pNIPAAM polymer brushes.[24]

The swelling process showed to be less affected by temperature differences. However, for this process two consecutive phases for increased ambient temperature could be observed. As the LCST was approached to the ambient temperature, these became more and more pronounced, leading to a time delay of up to 20 ms before the actual, exponential transition was initiated and took place.

The observed properties show that the phase transition of thermoresponsive polymer networks, as herein studied on pNIPAAM, can be externally controlled by changing parameters as ambient temperature, heating strength or duration. This knowledge could serve, amongst others, in the arising field of optically driven soft robotics where such an externally manageable, versatile material is already used in various applications as for example in thermally actuable valves in micro fluidic devices [23] or for optically manoeuvrable microgel constructs mimicking the swimming of microorganisms [9].

The results of this work have shown that the phase transition of such small hydrogel architectures is rather complex. In further experiments, one could examine more precisely which mechanisms underlie the transition, in particular which ones are responsible for the two superimposed processes for the increased heating periods in detail.

6. Literature

1. Materials in LEGO® elements - Sustainability - LEGO.com DE. https://www.lego.com/en-de/sustainability/product-safety/materials/.

2. Gu, Y., Zhao, J. & Johnson, J. A. Polymer Networks: From Plastics and Gels to Porous Frameworks. *Angew. Chemie - Int. Ed.* **59**, 5022–5049 (2020).

3. Hoffman, A. S. Hydrogels for biomedical applications. *Adv. Drug Deliv. Rev.* **64**, 18–23 (2012).

4. Diehl, F. *et al.* Plasmonic nanomaterials with responsive polymer hydrogels for sensing and actuation. *Chem. Soc. Rev.* 3926–3963 (2022) doi:10.1039/d1cs01083b.

5. Mateescu, A., Wang, Y., Dostalek, J. & Jonas, U. Thin hydrogel films for optical biosensor applications. *Membranes (Basel).* **2**, 40–69 (2012).

6. Harmon, M. E., Kuckling, D. & Frank, C. W. Photo-Cross-Linkable PNIPAAm Copolymers. 2. Effects of Constraint on Temperature and pH-Responsive Hydrogel Layers. *Macromolecules* **36**, 162–172 (2003).

7. Junk, M. J. N., Ilke, A., Menges, B. & Jonas, U. Analysis of optical gradient profiles during temperature- and salt-dependent swelling of thin responsive hydrogel films. *Langmuir* **26**, 12253–12259 (2010).

8. Schenderlein, H., Voss, A., Stark, R. W. & Biesalski, M. Preparation and characterization of light-switchable polymer networks attached to solid substrates. *Langmuir* **29**, 4525–4534 (2013).

9. Mourran, A., Jung, O., Vinokur, R. & Möller, M. Microgel that swims to the beat of light. *Eur. Phys. J. E* **44**, (2021).

10. Thérien-Aubin, H., Wu, Z. L., Nie, Z. & Kumacheva, E. Multiple shape transformations of composite hydrogel sheets. *J. Am. Chem. Soc.* **135**, 4834–4839 (2013).

11. Reinicke, S. *et al.* Smart hydrogels based on double responsive triblock terpolymers. *Soft Matter* 2648–2657 (2009) doi:10.1039/b900539k M4 - Citavi.

12. Junk, M. J. N., Berger, R. & Jonas, U. Atomic force spectroscopy of thermoresponsive photo-cross-linked hydrogel films. *Langmuir* **26**, 7262–7269 (2010).

13. Junk, M. J. N., Jonas, U. & Hinderberger, D. EPR spectroscopy reveals nanoinhomogeneities in the structure and reactivity of thermoresponsive hydrogels. *Small* **4**, 1485–1493 (2008).

14. Sun, S., Hu, J., Tang, H. & Wu, P. Chain collapse and revival thermodynamics of poly(N -isopropylacrylamide) hydrogel. *J. Phys. Chem. B* **114**, 9761–9770 (2010).

15. Uva, M. & Atrei, A. Surface Morphology at the Microscopic Scale, Swelling/Deswelling, and the Magnetic Properties of PNIPAM/CMC and PNIPAM/CMC/Fe3O4 Hydrogels. *Gels* **2**, 30 (2016).

16. Xue, W., Hamley, I. W. & Huglin, M. B. Rapid swelling and deswelling of thermoreversible hydrophobically modified poly(N-isopropylacrylamide) hydrogels prepared by freezing polymerisation. *Polymer (Guildf).* **43**, 5181–5186 (2002).

17. Lin, S. Y., Chen, K. S. & Liang, R. C. Thermal micro ATR/FT-IR spectroscopic system for quantitative study of the molecular structure of poly(N-isopropylacrylamide) in water. *Polymer (Guildf).* **40**, 2619–2624 (1999).

18. Ahmed, Z., Gooding, E. A., Pimenov, K. V, Wang, L. & Asher, S. A. UV Resonance Raman Determination of Molecular Mechanism of Poly(N-Isopropylacrylamide) Volume Phase Transition. *J. Phys. Chem. B* **113**, 4248–4256 (2009).

19. Nagase, K. Thermoresponsive interfaces obtained using poly(N-

isopropylacrylamide)-based copolymer for bioseparation and tissue engineering applications. *Adv. Colloid Interface Sci.* **295**, 102487 (2021).

20. Gammas, S. *et al.* Thermo-responsive polymer nanoparticles with a core-shell micelle structure as site-specific drug carriers. *J. Control. Release* **48**, 157–164 (1997).

21. Hageneder, S. *et al.* Responsive Hydrogel Binding Matrix for Dual Signal Amplification in Fluorescence Affinity Biosensors and Peptide Microarrays. *ACS Appl. Mater. Interfaces* **13**, 27645–27655 (2021).

22. Shimizu, T., Yamato, M., Kikuchi, A. & Okano, T. Cell sheet engineering for myocardial tissue reconstruction. *Biomaterials* **24**, 2309–2316 (2003).

23. Sershen, S. R. *et al.* Independent Optical Control of Microfluidic Valves Formed from Optomechanically Responsive Nanocomposite Hydrogels. *Adv. Mater.* **17**, 1366–1368 (2005).

24. Winkler, P. *et al.* Nanoplasmonic heating and sensing to reveal the dynamics of thermoresponsive polymer brushes. *Appl. Phys. Lett.* **107**, (2015).

25. Gallagher, S., Florea, L., Fraser, K. J. & Diamond, D. Swelling and shrinking properties of thermo-responsive polymeric ionic liquid hydrogels with embedded linear pNIPAAM. *Int. J. Mol. Sci.* **15**, 5337–5349 (2014).

26. Toma, M., Jonas, U., Mateescu, A., Knoll, W. & Dostalek, J. Active control of SPR by thermoresponsive hydrogels for biosensor applications. *J. Phys. Chem. C* **117**, 11705–11712 (2013).

27. Auer, S. K. *et al.* Rapid Actuation of Thermo-Responsive Polymer Networks: Investigation of the Transition Kinetics. *J. Phys. Chem. B* (2022) doi:10.1021/acs.jpcb.2c01160.

28. Jain, P. K., Lee, K. S., El-Sayed, I. H. & El-Sayed, M. A. Calculated absorption and scattering properties of gold nanoparticles of different size, shape, and composition: Applications in biological imaging and biomedicine. *J. Phys. Chem. B* **110**, 7238–7248 (2006).

29. Baffou, G. *et al.* Photoinduced heating of nanoparticle arrays. *ACS Nano* **7**, 6478–6488 (2013).

30. Berto, P., Mohamed, M. S. A., Rigneault, H. & Baffou, G. Time-harmonic optical heating of plasmonic nanoparticles. *Phys. Rev. B - Condens. Matter Mater. Phys.* **90**, (2014).

31. Huang, X., Jain, P. K., El-Sayed, I. H. & El-Sayed, M. A. Plasmonic photothermal therapy (PPTT) using gold nanoparticles. *Lasers Med. Sci.* **23**, 217–228 (2008).

32. Cherukuri, P., Glazer, E. S. & Curley, S. A. Targeted hyperthermia using metal nanoparticles. *Adv. Drug Deliv. Rev.* **62**, 339–345 (2010).

33. Quilis, N. G. *et al.* UV-Laser Interference Lithography for Local Functionalization of Plasmonic Nanostructures with Responsive Hydrogel. *J. Phys. Chem. C* **124**, 3297–3305 (2020).

34. Urban, A. S., Pfeiffer, T., Fedoruk, M., Lutich, A. A. & Feldmann, J. Single-step injection of gold nanoparticles through phospholipid membranes. *ACS Nano* **5**, 3585–3590 (2011).

35. Gianneli, M. *et al.* Dynamics of swollen gel layers anchored to solid surfaces. *Soft Matter* **4**, 1443–1447 (2008).

36. Quilis, N. G. *et al.* Tunable laser interference lithography preparation of plasmonic nanoparticle arrays tailored for SERS. *Nanoscale* **10**, 10268–10276 (2018).

37. Lamy de la Chapelle, M. *et al.* New Gold Nanoparticles Adhesion Process Opening the Way of Improved and Highly Sensitive Plasmonics Technologies. *Plasmonics* **8**, 411–415 (2013).

38. Sanders, W. C. *Atmoic Force Microscopy: Fundamental Concepts and Laboratory Investigations (1st ed.)*. vol. 148 (CRC Press, 2019).

39. Chatterjee, S., Gadad, S. S. & Kundu, T. K. Atomic force microscopy: A tool to unveil the mytery of biological systems. *Resonance* **15**, 622–642 (2010).

40. Jandt, K. D. Atomic force microscopy of biomaterials surfaces and interfaces. *Surf.*

Sci. **491**, 303–332 (2001).

41. Haugstad, G. *Atomic force microscopy*. *Informacije MIDEM* vol. 30 (John Wiley & Sons, Inc., 2012).

42. Raether, H. *Surface Plasmons on Smooth and Rough Surfaces and on Gratings*. (Springer Berlin, Heidelberg, 1988). doi:10.1007/BFb0048317.

43. Huang, C.-J., Jonas, U., Dostálek, J. & Knoll, W. Biosensor platform based on surface plasmon-enhanced fluorescence spectroscopy and responsive hydrogel binding matrix. *Opt. Sensors 2009* **7356**, 735625 (2009).

44. Otto, A. Excitation of nonradiative surface plasma waves in silver by the method of frustrated total reflection. *Zeitschrift für Phys.* **216**, 398–410 (1968).

45. Kretschmann, E. & Raether, H. Radiative Decay of Non Radiative Surface Plasmons Excited by Light. *Zeitschrift fur Naturforsch. - Sect. A J. Phys. Sci.* **23**, 2135–2136 (1968).

46. Lawrence, C. R., Geddes, N. J., Furlong, D. N. & Sambles, J. R. Surface plasmon resonance studies of immunoreactions utilizing disposable diffraction gratings. *Biosens. Bioelectron.* **11**, 389–400 (1996).

47. Dostálek, J. & Knoll, W. Biosensors based on surface plasmon-enhanced fluorescence spectroscopy (Review). *Biointerphases* **3**, FD12–FD22 (2008).

48. Homola, J. & Piliarik, M. *Surface Plasmon Resonance Based Sensors*. vol. 4 (Springer Berlin Heidelberg, 2006).

49. Pockrand, I., Swalen, J. D., Gordon II, J. G. & Philpott, M. R. Surface plasmon spectroscopy of organic monolayer assemblies. *Surf. Sci.* **74**, 237–244 (1977).

50. Lechner, B. Rolling circle amplification for plasmonic biosensors. (University of Natural Resources and Life Sciences, Vienna, 2020).

51. Tanaka, T., Sato, E., Hirokawa, Y., Hirotsu, S. & Peetermans, J. Critical Kinetics of Volume Phase Transition of Gels. *Phys. Rev. Lett.* **55**, 2455–2458 (1985).

52. Jia, D. & Muthukumar, M. Theory of Charged Gels: Swelling, Elasticity, and

Dynamics. *Gels* **7**, (2021).

53. Toomey, R., Vidyasagar, A. & Ortiz, O. Swelling Behavior of Thin Hydrogel Coatings. in *Functional Polymer Films* 649–667 (John Wiley & Sons, Ltd, 2011). doi:https://doi.org/10.1002/9783527638482.ch19.

54. Erman, B. & Flory, P. J. Critical Phenomena and Transitions in Swollen Polymer Networks and in Linear Macromolecules. *Macromolecules* **19**, 2342–2353 (1986).

7. List of Figures

8. List of Tables

9. Appendix

The results of this work were published as a journal article in **The Journal of Physical Chemistry B** on the 14th of April 2022 with the title *"Rapid Actuation of Thermo-Responsive Polymer Networks: Investigation of the Transition Kinetics"* (doi: 10.1021/acs.jpcb.2c01160.), which is presented in the following.

THE JOURNAL OF PHYSICAL CHEMISTRY B
A JOURNAL OF THE AMERICAN CHEMICAL SOCIETY

pubs.acs.org/JPCB

Article

Rapid Actuation of Thermo-Responsive Polymer Networks: Investigation of the Transition Kinetics

Simone K. Auer, Stefan Fossati, Yevhenii Morozov, Dario Cattozzo Mor, Ulrich Jonas, and Jakub Dostalek*

Cite This: *J. Phys. Chem. B* 2022, 126, 3170–3179

Read Online

ACCESS | Metrics & More | Article Recommendations | Supporting Information

ABSTRACT: The swelling and collapsing of thermo-responsive poly(*N*-isopropylacrylamide)-based polymer (pNIPAAm) networks are investigated in order to reveal the dependency on their kinetics and maximum possible actuation speed. The pNIPAAm-based network was attached as thin hydrogel film to lithographically prepared gold nanoparticle arrays to exploit their localized surface plasmon resonance (LSPR) for rapid local heating. The same substrate also served for LSPR-based monitoring of the reversible collapsing and swelling of the pNIPAAm network through its pronounced refractive index changes. The obtained data reveal signatures of multiple phases during the volume transition, which are driven by the diffusion of water molecules into and out of the network structure and by polymer chain re-arrangement. For the micrometer-thick hydrogel film in the swollen state, the layer can respond as fast as several milliseconds depending on the strength of the heating optical pulse and on the tuning of the ambient temperature with respect to the lower critical solution temperature of the polymer. Distinct differences in the time constants of swelling and collapse are observed and attributed to the dependence of the cooperative diffusion coefficient of polymer chains on polymer volume fraction. The reported results may provide guidelines for novel miniature actuator designs and micromachines that take advantages of the non-reciprocal temperature-induced volume transitions in thermo-responsive hydrogel materials.

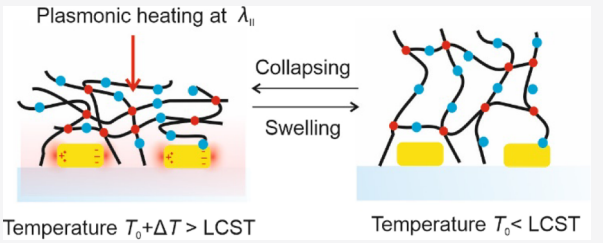

INTRODUCTION

Responsive polymers represent an important class of materials that serve in a broad range of applications spanning from drug delivery,[1] switchable biocompatible coatings,[2] and advanced biointerfaces in bioanalytical devices[3,4] to active materials driving miniature actuators and micromachines.[5,6] Responsive polymers are designed to change their properties with various stimuli, among which temperature is one of the most commonly used. The majority of thermo-responsive polymers possess a lower critical solution temperature (LCST), below which they exhibit a hydrophilic character, which results in cross-linked polymer networks in an open structure that incorporates high amounts of water molecules. Upon increasing the temperature above the LCST, the polymer chains switch to a hydrophobic state and yield a more compact conformation by expelling water from their proximity. A very prominent example for thermo-responsive LCST polymers is poly(*N*-isopropylacrylamide) (pNIPAAm), but many other materials with such a LCST behavior have been developed over time.[7]

Thermo-responsive polymers have been exploited as polymer brushes or networks forming hydrogels after swelling with water in the form of thin films attached to the surface of solid substrates and colloidal particles[8−10] or as microgels with spherical[11] and more complex shapes.[12−15] One of the key characteristics of devices prepared from LCST hydrogels is the speed, with which they can respond to changes in temperature. For example, surface-attached hydrogel microstructures based on pNIPAAm were developed to actuate microfluidic valves that can be reversibly switched in 5 s.[16] The same material was employed as thin microgel ribbons[12,17] to perform optically actuated locomotion by cycling through non-reciprocal morphing in a period of about 1 s. Rapid disassembly of metallic nanoparticle aggregates that are capped with pNIPAAm brushes was reported for mechanical release of energy on a μs time scale via a spring-loaded mechanism.[18]

In general, the response time of actuated thermo-responsive polymer devices with hydrogel network and brush architectures depends on various factors, like the speed of the individual chain response with respect to its solvation state, their collective conformation switching, and on the diffusion of water molecules in and out of the network structure. The latter effect is particularly detrimental with increasing size of the

Received: February 17, 2022
Revised: March 30, 2022
Published: April 14, 2022

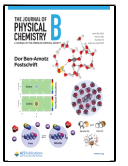

https://doi.org/10.1021/acs.jpcb.2c01160
J. Phys. Chem. B 2022, 126, 3170−3179

hydrogel structures, and it is worth noting that recently developed hydrogel composite materials allow overcoming this limitation in part, owing to its highly porous structure.[5]

The swelling and collapse kinetics of pNIPAAm-based brushes and networks are commonly investigated by changing the bulk temperature of the aqueous environment comprising the studied specimen.[19] However, the temperature variation under these conditions is typically slow due to the large heat capacity of the macroscopic volume, which limits the accessible kinetic range. Faster modulation could be achieved by more local heating approaches, for example, based on thin resistive ITO microheaters[4] or particularly via plasmonic heating.[20] Plasmonic heating relies on the optical excitation of localized surface plasmon (LSP) modes on the surface of metallic nanostructures, which originate from collective oscillations of the electron density and the associated electromagnetic field. These resonances optically probe the close vicinity of the metallic nanostructure and dissipate to heat via Ohmic losses in the metal. Therefore, metallic nanostructures can serve as efficient optically controlled local heat sources.[21] In conjunction with thermo-responsive polymers, such plasmonic heaters were implemented by loading microgels from pNIPAAm polymer networks with synthetically made metallic nanorods[13] or by capping individual metallic nanoparticles with pNIPAAm chains when attached to a substrate[22] or used in the form of a colloid.[18]

The swelling and collapse kinetics of 30 nm-thick pNIPAAm brushes on lithographically fabricated plasmonic nanoparticles demonstrated a single-exponential behavior on a time scale of 0.16 ms.[20] Contrary to this, the pNIPAAm polymer network forming a hydrogel film with a thickness of 600 nm revealed more complex swelling and collapse kinetics. The hydrogel layer responded in two phases with the faster component exhibiting a response time below 100 ms and the slower process occurring on a time scale of seconds.[4] These signatures have been attributed to the effect of water diffusion into and out of the structure and subsequent slower rearrangement and collective motion of interconnected polymer chain segments. The related effect of chain entanglement and other intrachain and interchain interactions was ascribed to the occurrence of hysteresis in the swelling and collapsing process for a pNIPAAm brush upon slowly varying temperature around the LCST.[23]

In this work, we apply rapid plasmonic heating in order to investigate differences in the swelling and collapsing kinetics of pNIPAAm networks on a time scale that was, so far, used only with thin brush architecture.[20] We further study these transitions as a function of the strength of the local temperature increase, the heating pulse duration, and ambient temperature offset with respect to the LCST of the polymer. The external parameters are controlled to determine the ultimate actuation speed and to devise possible routes for efficient and rapidly operated micromachines and nanomachines.

METHODS

Preparation of Au Nanoparticle Arrays. A He−Cd laser (IK 3031 R−C from Kimmon, Japan) emitting at λ = 325 nm with 4 mW was employed. The coherent beam was expanded with a spatial filter consisting of a pinhole (10 μm) and ×40 microscope lens. The expanded beam was collimated by using a fused silica lens (f = 1 m), and its intensity was measured to be 10 μW cm^{-2}. Au nanoparticle arrays were prepared as previously reported by the use of the two-beam laser interference lithography with Lloyd's configuration.[24] Briefly, 2 nm-thick Cr and 50 nm-thick Au layers were evaporated on top of BK7 glass slides with a size of 25 × 25 mm (HHV AUTO 306 from HHV Ltd, UK, in a vacuum better than 10^{-6} mBar). Subsequently, a 100 nm-thick layer of S1805 positive photoresist (from micro-resist technology GmbH, diluted 1:2 with propylene glycol monomethyl ether acetate) was spun at a spin rate of 4500 rpm for 45 s. Soft baking of the resist was conducted at 98 °C for 2 min. The angle of the interfering beams in Lloyd's configuration was set to 21.17°, yielding a period of Λ = 450 nm, and the dose was set to 4.2 and 2.4 J cm^{-2} in the two orthogonal directions. The parameters were adjusted to obtain arrays of resist features exhibiting an elliptical footprint with a distinct short axis length $D^{\perp}$ and a long axis length $D^{\parallel}$ after immersing the substrate in the AZ303 developer (1:15 ratio deionized water). Such a resist mask was transferred to the underlying gold layer using a dry etching process consisting of bombardment of the surface with argon ions (Roth & Rau IonSys 500, Germany, 5 × 2 min etching with 2 min pauses in between). Resist-free Au nanoparticles were finally obtained by exposing the substrate to an oxygen plasma process.

AFM Analysis of Au Nanoparticle Arrays. The topography of the prepared arrays of Au nanoparticles was measured by using atomic force microscopy (PicoPlus from Molecular Imaging, Agilent Technologies, Germany) with tapping-mode tips PPP-NCHR-50 (Nanosensors, Switzerland). The obtained images were processed in open-source software Gwyddion (version 2.47 from gwyddion.net).

Synthesis of pNIPAAm. The pNIPAAm-based terpolymer was synthesized using *N*-isopropylacrylamide (NIPAAm), methacrylic acid (MAA), and *N*-(4-benzoylphenyl)acrylamide (BPAAm)[25] (94:5:1 ratio) monomers according to the procedures previously reported.[26,27] A 50 mL Schlenk flask was charged with 1,4-dioxane (20 mL). Oxygen was then removed by degassing the solvent and flushing with argon. This procedure was repeated three times, followed by the addition of NIPAAm (17.8 mmol, 2.01 g), MAA (1.2 mmol, 0.1 g), and BPAAm (0.18 mmol, 0.045 g). After stirring the solution at room temperature for 30 min, AIBN (0.22 mmol, 0.036 g) was added, and the solution was heated up 60 °C for 18 h. After cooling to room temperature, the resulting polymer was precipitated in ice-cold Et_2O, filtered off, and washed again with Et_2O several times. The polymer was isolated by drying at 50 °C under reduced pressure, and the yield was 77% (1.66 g).

Preparation of the pNIPAAm-Based Hydrogel Layer. In order to attach the hydrogel to the Au nanoparticle arrays, their surface was modified with benzophenone moieties by overnight reaction with 1 mM benzophenone disulfide (synthesized as described before[25]) dissolved in DMSO. Subsequently, a pNIPAAm-based polymer dissolved in ethanol (2 wt %) was spun (2000 rpm for 2 min) over the Au nanoparticle array surface followed by drying overnight in a vacuum (T = 50 °C). The polymer layer was then simultaneously cross-linked and attached to the surface by irradiation with UV light (dose of 2 J/cm^2 at λ = 365 nm). The thickness of the hydrogel layer attached to the Au nanoparticles in a dry and swollen state was measured using an in-house sensor system based on surface plasmon resonance (SPR) (see Supporting Information, part 1).

Optical Setup for LSPR Tracking and Plasmonic Heating. An in-house developed optical instrument is

https://doi.org/10.1021/acs.jpcb.2c01160
J. Phys. Chem. B 2022, 126, 3170−3179

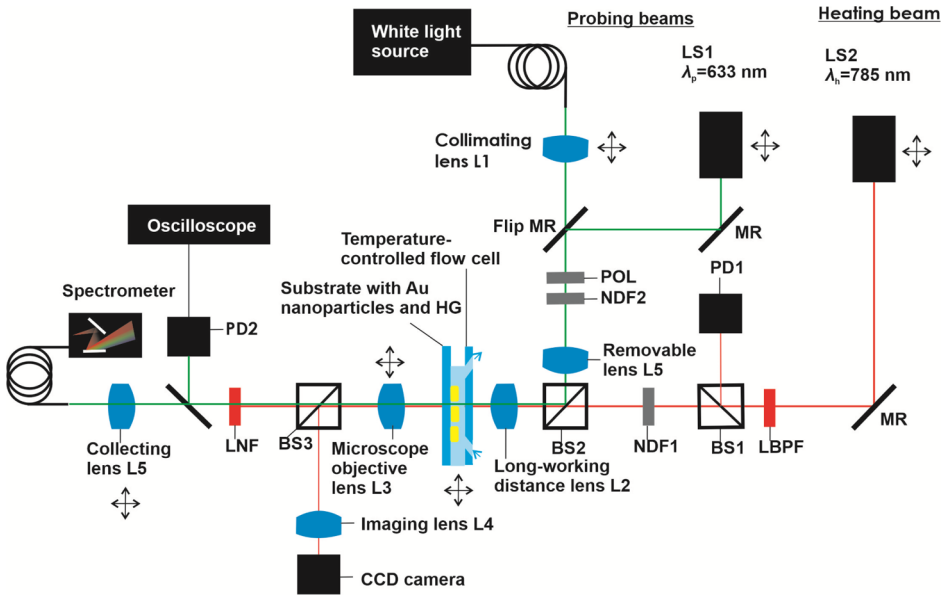

Figure 1. Optical setup employed for the combined wide-field optical microscopy observation of the surface carrying arrays of Au nanoparticles with a thermo-responsive hydrogel (HG) overlayer and for the beam alignment, transmission wavelength spectroscopy-based recording of LSPR spectra, and for the optical heating and monitoring of rapid LSPR kinetics.

schematically shown in Figure 1. The glass substrate with arrays of Au nanoparticles and a pNIPAAm-based hydrogel layer on the top was clamped to a flow cell. The flow cell chamber was formed by using a PDMS gasket and a transparent glass lid, which was contacted with a Peltier device in order to control the ambient bulk temperature T_0 (operated with a temperature controller, wavelength electronics, model LFI-3751, USA). The flow cell with the clamped sample carrying the pNIPAAm-based hydrogel layer mounted on a set of XYZ linear stages was optically probed with a series of beams that passed through the fixed long-working distance objective lens L2 (Mitutoyo MPlan Apo 50x/0.55, ∞/0 f = 200, Japan). The polychromatic beam emitted from a halogen lamp (LSH102 LOT-Oriel, Germany) was coupled to an optical fiber (Thorlabs, UK), delivered to a collimator L1 (Thorlabs, UK), and made to pass through a polarizer POL (B.Halle, Germany). A monochromatic beam at a probing wavelength of λ_p = 633 nm emitted from a HeNe laser (LS1, Melles Griot stabilized HeNe Laser system 633 nm, USA) was used, and a monochromatic beam at a different heating wavelength of λ_h = 785 nm (LS2, Toptica Photonics iBeam smart WS wavelength-stabilized diode laser 785 nm, 250 mW, Germany) was introduced into the system. The intensity of the heating beam I_h was chopped, made to pass through a band pass filter LBPF (FB780-10, Thorlabs, United States), and by using a splitter BS1, its intensity was monitored using a photodiode PD1. The polychromatic and monochromatic beams were merged by using a splitter BS2 and launched at the substrate with the pNIPAAm-based layer in the temperature-controlled flow cell. The transmitted beams were recollimated with a lens L3. By using a splitter BS3 (splitting rate 90:10, Thorlabs, UK) and lens L4 (Schneider Kreuznach Unifoc Component 4/35, FL 35, Germany), the surface of the pNPAAm-based layer was imaged using a CCD camera (piA1000-48ag, Basler AG, Germany). The beams that passed through the other arm of BS3 were spectrally filtered with a notch filter LNF (NF785-33, Thorlabs, UK) and were delivered either to a photodiode PD2 (probing beam at λ_p) or collected by using a lens L5 (FL 90) and launched to an optical fiber (Ocean Optics, USA) and analyzed using a spectrometer (Andor Technology, Shamrock 303 Spectrometer, UK) (polychromatic beam). The intensity of the monochromatic probing beam at λ_p was analyzed by using an oscilloscope (Agilent Technologies, DSO 1004A 60 MHz 2GSa/s, United States), where the signal from PD1 (intensity of heating beam at λ_h) served as a trigger and PD2 (intensity of the probing beam at λ_p) as an input. The long-distance working lens L2 was used to focus the polychromatic and monochromatic beams on the pNIPAAm-based layer surface. The focus was checked with the CCD camera and the circular areas irradiated with the beams were aligned to overlap and set to the same diameter of 30 μm. For the (static) measurement of LSPR, the spectra acquired by using a polychromatic beam and spectrometer were normalized with those measured on an area of the substrate that did not carry the Au nanoparticle arrays. The measurement of the swelling and collapsing kinetics was performed by using an oscilloscope configuration, and the averaging of the sensorgrams by a factor of 256 was used. The flow cell was connected to a peristaltic pump (Ismatec, Switzerland) in order to transport water across the surface of the pNIPAAm-based hydrogel layer.

Numerical Simulations. LSPR transmission spectra were simulated with the finite-difference time-domain method (Lumerical Inc., Canada). Following geometrical parameters for arrays of gold nanoparticles were used: an elliptical footprint with a short axis of $D^{\perp}$ = 200 nm, a long axis of $D^{\parallel}$ = 260 nm, and a height of 50 nm arranged in rectangular arrays with a period of Λ = 450 nm. Below the gold nanoparticles, a Cr layer of 2 nm was assumed. The BK7 glass interface (with a refractive index of 1.5) was carrying a dielectric layer with a thickness of 845 nm and refractive index n_h = 1.35 (representing the pNIPAAm-based hydrogel in the swollen state) or a thickness of 105 nm and refractive index n_h = 1.42 (representing the pNIPAAm-based hydrogel in the collapsed state). As a superstrate, water medium with a refractive index of 1.33 was set. A plane wave made normally incident on the

https://doi.org/10.1021/acs.jpcb.2c01160
J. Phys. Chem. B 2022, 126, 3170−3179

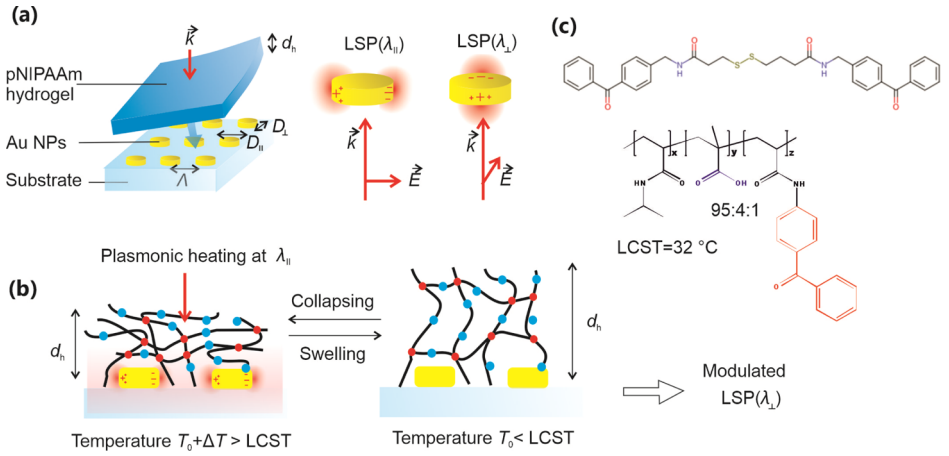

Figure 2. Schematics of the (a) substrate with arrays of elliptical Au nanoparticles that exhibit distinct LSPR wavelengths and that carry thermo-responsive poly(*N*-isopropylacrylamide)-based (pNIPAAm) hydrogel layers on the top. (b) pNIPAAm polymer network swelling and collapsing by using the temperature stimulus and (c) chemical structure of the benzophenone disulfide linker and used pNIPAAm-based terpolymer.

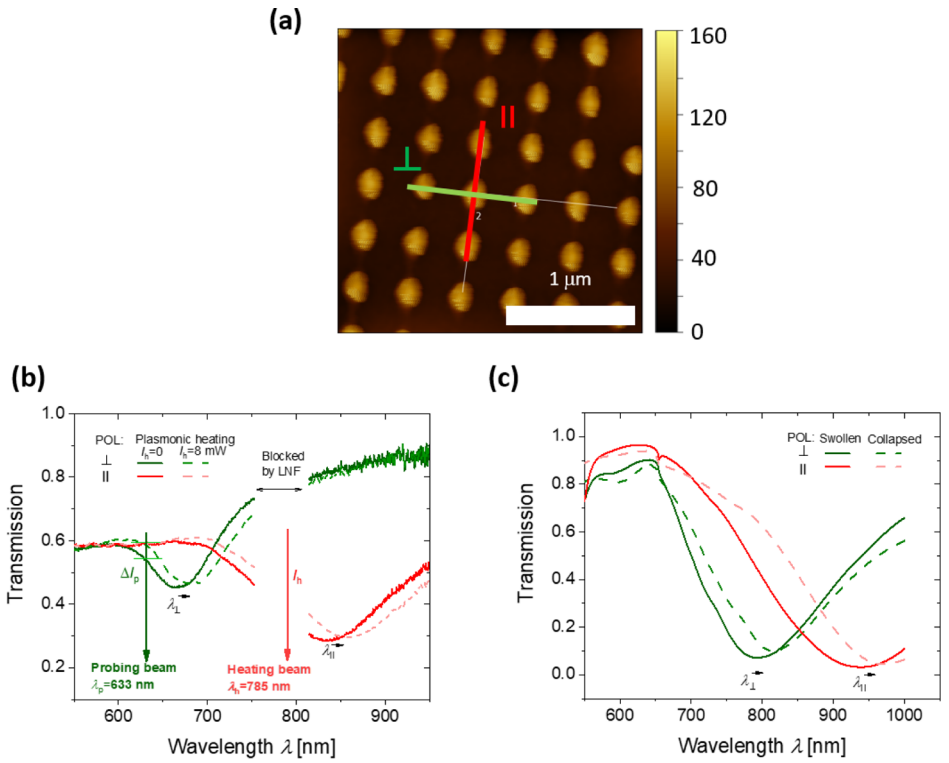

Figure 3. (a) Topography of the prepared Au nanoparticle arrays and comparison of (b) measured and (c) simulated LSPR transmission spectra when the attached pNIPAAm-based hydrogel layer is swollen and collapsed (assuming the refractive index of n_h = 1.35 and 1.48, respectively).

structure was used as an excitation source. Periodic (along the *x*- and *y*-axis) and perfectly matched layer absorbing (on the *z*-axis 1.2 μm above and below the structure) boundary conditions were applied. Au and Cr optical properties were taken from the literature.[28,29]

RESULTS AND DISCUSSION

Rapid actuation of pNIPAAm-based, thermo-responsive polymer networks swollen with water was achieved by plasmonic heating of metallic nanostructures. As schematically shown in Figure 2a, these metallic nanostructures were attached to the glass substrate and a layer of the pNIPAAm-based hydrogel was anchored to their top. In order to simultaneously employ the metallic nanostructure for rapid actuation of the thermo-responsive network and for the measurement of its swelling and collapse kinetics, periodic arrays of Au nanoparticles with an elliptical footprint were prepared. On these nanoparticles, LSPs at distinct resonant wavelengths of $\lambda^{\perp}$ nm and $\lambda^{\parallel}$ can be excited when rotating the polarization of the incident beam perpendicular ⊥ or parallel ∥ to their long axis. The LSPs at shorter wavelength $\lambda^{\perp}$ were then used for the probing of refractive index changes that accompany the swelling and collapse of the pNIPAAm-based polymer network. The LSPs at longer wavelength $\lambda^{\parallel}$ were utilized for the coupling of a heating beam and subsequent local dissipation of its energy via the Ohmic losses (see Figure 2b).

https://doi.org/10.1021/acs.jpcb.2c01160
J. Phys. Chem. B 2022, 126, 3170−3179

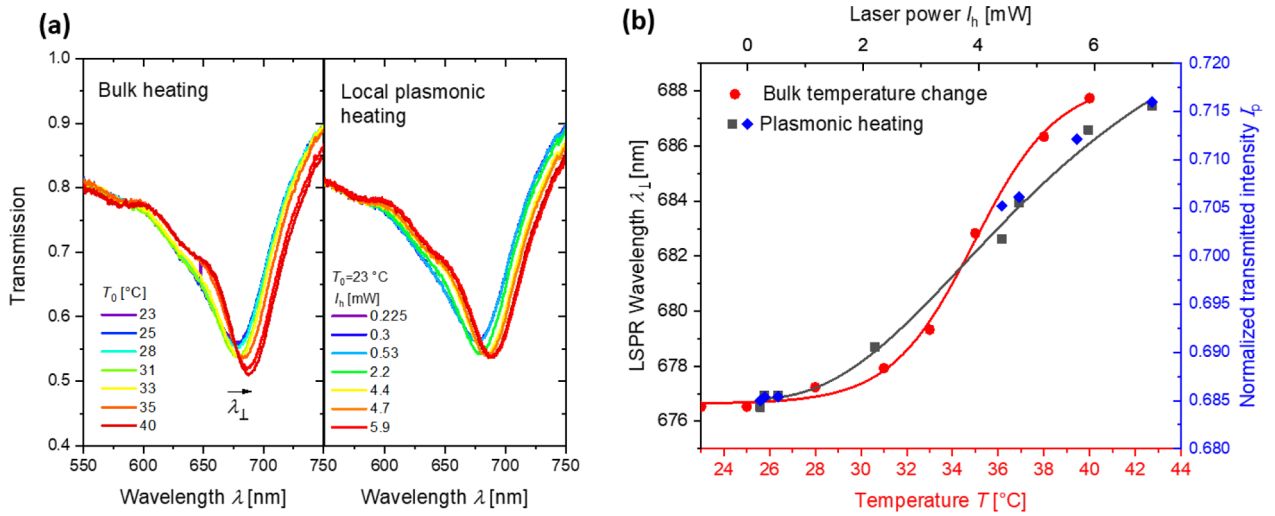

Figure 4. (a) LSPR spectra centered at $\lambda^{\perp}$ measured for variable bulk temperature T_0 and the same LSPR spectra acquired for increasing intensity of the heating beam. (b) Comparison of the LSPR shifts, enabling calibration of the temperature changes due to the plasmonic heating. The measured data are shown as symbols, and lines are sigmoid function fits that are overlaid to match the response at $I_h = 0$ and at the inflection point.

Preparation of pNIPAAm Networks on the Plasmonic Substrate. Periodic arrays of elliptical Au nanoparticles were prepared by using UV laser interference lithography in combination with a dry etching step. As can be seen from the AFM micrographs in Figure 3a, they exhibited a short axis length of $D^{\perp}$= (200 ± 10) nm, a long axis length of $D^{\parallel}$= (260 ± 20) nm, a height of h = 50 nm, and the period was set to Λ = 450 nm. For these parameters, the spectral position of LSPR bands could be tuned close to the heating beam wavelength (λ_h = 785 nm) and probing beam wavelength (λ_p = 633 nm). The surface of the Au nanoparticles was chemically modified with a self-assembled monolayer of disulfide molecules with a photo-reactive benzophenone headgroup (Figure 2c). The pNIPAAm-based polymer layer was deposited on top with a (dry) thickness of d_h = 104 nm. The terpolymer carried a small amount of negatively charged methacrylic acid groups promoting swelling. In addition, photo-reactive benzophenone groups served for simultaneous cross-linking and attaching to Au nanoparticles upon irradiation with UV light. When the UV-cross-linked layer was contacted with water, the polymer network took up water molecules, leading to its swelling and increase in the thickness to d_h = 843 nm at room temperature T_0 = 24 °C. Surface plasmon resonance combined with optical waveguide spectroscopy (see Supporting Information S1) showed that the pNIPAAm-based hydrogel exhibits a refractive index of n_h = 1.48 when it is dry and decreases to 1.35 when it swells in water. By raising temperature above LCST to 40 °C, the thickness decreases by a factor of 4.7 and the refractive index increases to n_h = 1.42.[30]

LSPR Probing of the pNIPAAm Layer. After the attachment of the pNIPAAm-based polymer network atop the Au nanoparticle arrays, the substrate was clamped against a flow cell and water was transported over its surface. As can be seen in Figure 3b, the excitation of the LSPs with their dipole moment aligned along the short and long axes manifests itself as two spectrally distinct dips in the measured wavelength transmission spectrum. For the polarization of the incident optical beam aligned perpendicular to the long axis, the LSPR occurs at a wavelength of about $\lambda^{\perp}$ = 650 nm, when the pNIPAAm-based hydrogel layer is kept at room temperature. When the polarization is rotated by 90° to align with the long axis of the elliptical nanoparticles, the LSPR is switched to about $\lambda^{\parallel}$ = 850 nm. This LSPR dip was tuned close to the wavelength of the near-infrared heating beam (λ_h = 785 nm). When irradiating the surface with the heating beam power of I_h = 8 mW, both LSPR dips shift to longer wavelengths due to the induced collapse of the pNIPAAm-based hydrogel that results in the compacting of the thermo-responsive polymer network on the nanoparticle surface. It leads to an increase in the polymer volume fraction Φ, and thus, it is associated with a proportional increase in the refractive index n_h (see also Supporting Information section 7). This effect is ascribed to the local change in temperate ΔT that exceeds LCST of the pNIPAAm polymer network. In order to relate the spectral shifts of LSPR bands to variations in refractive index n_h and thickness d_h of the pNIPAAm-based polymer network film, numerical simulations were carried out. Data presented in Figure 3c predict the shift in the LSPR wavelength by about $\Delta\lambda^{\perp}/\Delta n_h$ = 183 nm/RIU and $\Delta\lambda^{\parallel}/\Delta n_h$ = 238 nm/RIU. Based on these values, the measured spectral shifts of $\Delta\lambda^{\perp}$ = 20 nm and $\Delta\lambda^{\perp}$ = 26.1 nm correspond to a change in the refractive index of the film of Δn_h = 0.11 RIU. This value translates to the swelling ratio change of a flat film of 7.5, which is in the range of the one measured previously for the same type of polymer and cross-linking.[30] It is worth of noting that the simulated LSPR spectra qualitatively agree with the measured ones, but the LSPR wavelengths are red-shifted with respect to the measured ones by about 150 nm. This discrepancy can be ascribed to the over-estimation of Au nanoparticle short- and long-axis lengths $D^{\perp}$ and $D^{\parallel}$ due to the convolution of tip geometry of the used AFM tip with the particle geometry.

Let us point out that the herein-measured LSPR shifts due to temperature changes can be dominantly attributed to swelling and collapsing of the investigated pNIPAAm-based hydrogel. Other effects are significantly less pronounced and are associated with optical changes at least one order of magnitude weaker. As discussed in Supporting Information in detail (Section 2), these effects include thermal expansion of the substrate, modulating the period of the gold nanoparticle arrays Λ, and temperature variations of the refractive index of the glass substrate and water.

https://doi.org/10.1021/acs.jpcb.2c01160
J. Phys. Chem. B 2022, 126, 3170−3179

Calibration of Plasmonic Heating-Induced Local Temperature Changes. The developed optical system was calibrated by relating the heating beam intensity I_h (that was focused on a circular area with a diameter of 30 μm) to the local increase in temperature ΔT. Figure 4a compares shifts of the resonant wavelength $\lambda^{\perp}$ in LSPR transmission spectra caused by a change in the bulk ambient temperature T_0 (induced by a Peltier device) with those locally induced (through the effect of plasmonic heating) by gradually increasing the continuous irradiation power I_h of the heating beam from 0 to 5.9 mW. Both graphs show a red shift of the LSPR absorption band of similar magnitude that is ascribed to the gradual collapse of the pNIPAAm-based hydrogel. Assuming that the effect of the temperature-induced decrease in the refractive index of water and potential changes in the period of the nanoparticle arrays due to thermal expansion can be omitted, the thermally and irradiation-induced LSPR wavelength shifts are related in Figure 4b. The measured data were fitted with sigmoid function and overlaid to match the response at I_h = 0 and at the inflection point. This relationship is used to convert the heating beam irradiation power at λ_h to the local temperature increase on the surface of the nanoparticles ΔT in order to show which applied laser powers I_h correlate with specific temperature changes ΔT. For the maximum used power of I_h = 7 mW, a temperature increase as high as ΔT = 15 K was determined. It should be noted that the dependence of the LSPR wavelength $\lambda^{\perp}$ on the bulk temperature T_0 exhibits more abrupt changes in the vicinity to LCST than that measured with the plasmonic heating. This can be attributed to the possible gradient in the local temperature increase ΔT due to the Gaussian profile of the heating beam intensity irradiating a footprint with a diameter of 30 μm.

Moreover, the monitoring of swelling and collapse of the pNPAAm-based polymer network was utilized by probing the LSPR changes at a fixed wavelength of λ_p = 633 nm. Then, the red shift of the LSPR band was manifested as an increase in the transmitted intensity of the beam I_p (see Figure 3b). As it follows the same trend as the variations in resonant wavelength $\lambda^{\perp}$ (see right axis in Figure 4b), it was used for the monitoring of the fast actuation of pNIPAAm hydrogel by using an oscilloscope at the output.

pNIPAAm Network Swelling and Collapsing Kinetics. In order to measure the kinetics of the swelling and collapse of the pNIPAAm-based hydrogel layer, the developed optical system was configured for the measurement of LSPR changes at λ_p with an oscilloscope, upon applying a series of short pulses of the increased heating beam intensity I_h. Let us note that the temperature changes ΔT follow the variations in the irradiation beam intensity I_h faster than millisecond, as can be seen from the quick decrease in I_p upon switching on the heating beam (t = 0 in Figure 5a,b) and an increase in I_p when the beam is switched off (t = 20 in Figure 5a,b). These abrupt changes can be ascribed to rapid variations in the refractive index of water, which follows the opposite trend compared to that of the investigated pNIPAAm-based film. Similar response time can be estimated from theory when the used plasmonic heating with arrays of gold nanoparticles is in a collective heating regime[31] (see Section 2 in Supporting Information). After this initial phase, switching "on" the heating beam power I_h received by the sample at λ_h was accompanied with a gradual increase in the probing beam intensity I_p at λ_p. When the heating beam is set "off", a gradual decrease to original baseline

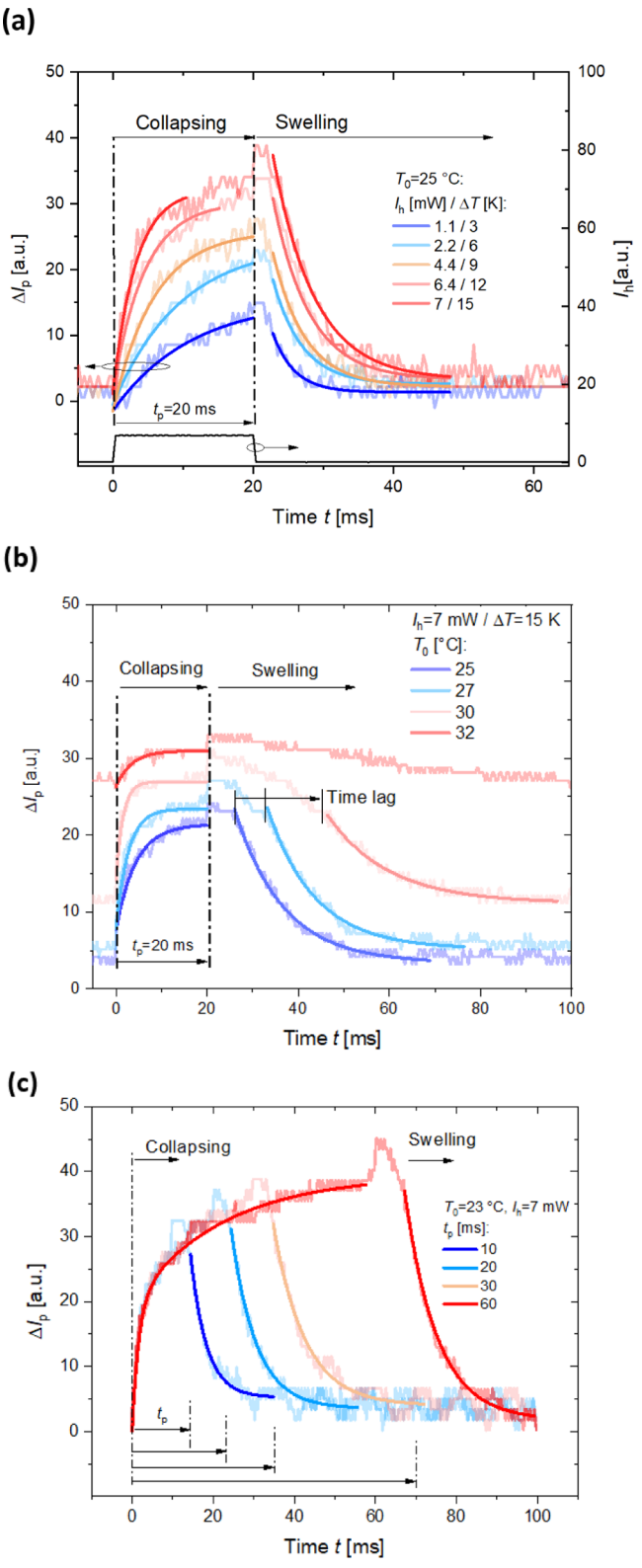

Figure 5. Recorded LSPR kinetics for the pNIPAAm-based polymer network collapse and swelling when (a) varying local temperature increase ΔT from below to above LCST, (b) increasing the bulk temperature T_0 to LCST and applying constant ΔT, and (c) for changing the time duration of the plasmonic heating pulse t_p. The measured data (presented as curve with light color) are fitted with exponential functions (shown as a curve with corresponding dark color).

https://doi.org/10.1021/acs.jpcb.2c01160
J. Phys. Chem. B 2022, 126, 3170−3179

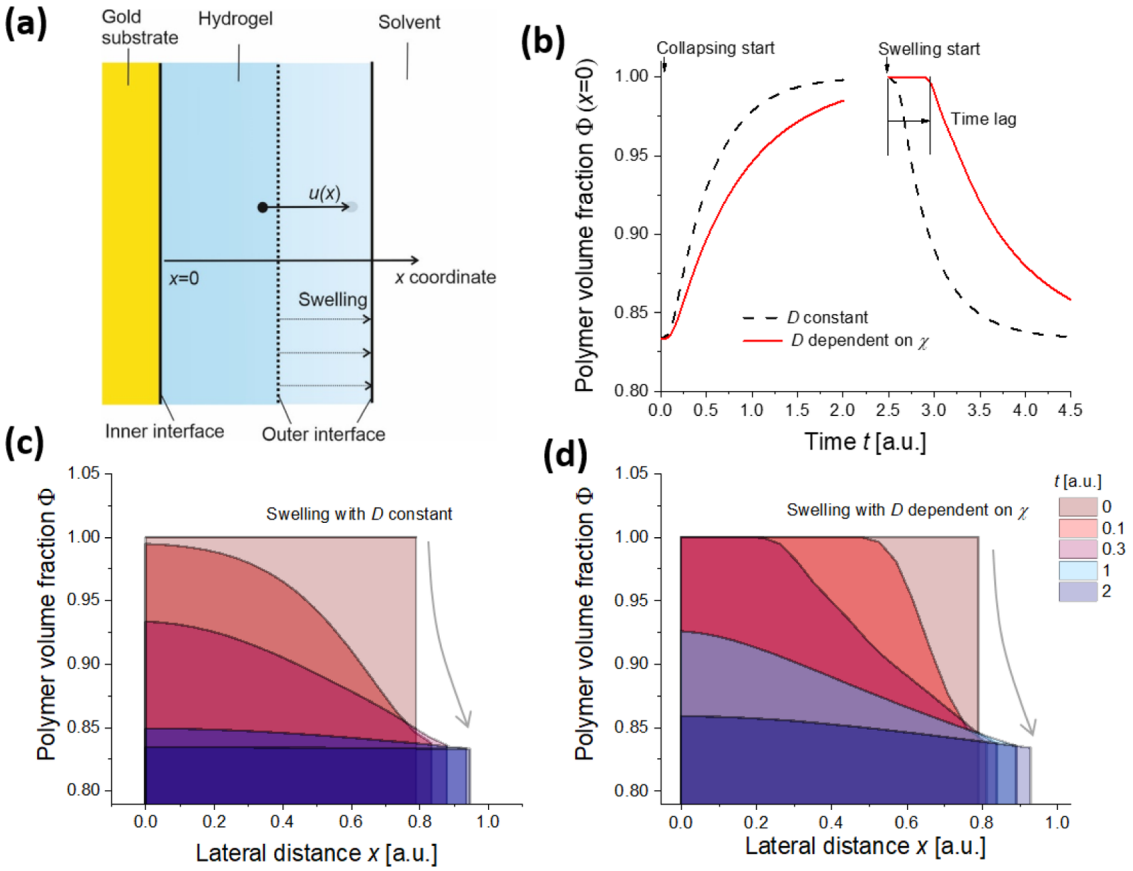

Figure 6. (a) Assumed geometry and definition of the displacement distance describing the swelling and collapsing process of an attached hydrogel layer. (b) Simulated time dependence of the polymer volume fraction Φ upon the collapsing and swelling process at the inner interface (x = 0). The spatial distribution of the polymer volume fraction upon the swelling process for the model with (c) constant D and (d) when taking into account its dependence on the Flory–Huggins parameter χ.

occurs. These changes follow the collapse and swelling of the pNIPAAm-based polymer networks through the induced refractive index variations Δn_h that are associated with changes in the polymer volume fraction Φ and probed by the LSP field confined on the surface of the Au nanoparticle arrays. Furthermore, considering the large thermal penetration depth into the medium within the characteristic time constant (see Supporting Information, section 4), we assume uniform temperature across the hydrogel layer.

In the first experiment, the bulk temperature of the substrate was set below the LCST to T_0 = 25 °C and the heating pulse strength was set to induce a local temperature increase of ΔT = 3, 6, 9, 12 and 15 K for a pulse duration of t_p = 20 ms. As can be seen in Figure 5a, the collapsing of the network is manifested as a gradual increase in the network density (monitored from LSPR changes associated with respective refractive index changes δn_h). Particularly, for the higher heating strength, the signal intensity kinetics slows down corresponding to approaching to the equilibrium. The collapsing speed increases with the heating strength (time constants of 9.6 and 3.3 ms were fitted with an exponential function for ΔT = 3 and 15 K, respectively). Contrary to the collapsing, the time dependence of the swelling phase does not change significantly with ΔT and can be well-fitted with an exponential function time constant of 4.8 ± 1 ms.

In the second experiment, the local heating strength was set fixed to the value of ΔT = 15 K and the bulk temperature was increased toward the LCST by setting T_0 = 25, 27, 30, and 32 °C for the pulse duration of t_p = 20 ms. The acquired response kinetics are presented in Figure 5b, and the collapsing phase reveals that when T_0 approaches the LCST, a faster compaction of the pNIPAAm-based hydrogel film occurs (shorter time constant of 1.5 ms was measured for T_0 = 30 °C). Interestingly, the subsequent swelling after turning off the heating beam shows a more complex behavior and it strongly slows down when T_0 approaches the LCST. Apparently, it exhibits kinetics consisting of two distinct phases. In the initial transition phase (occurring after the switching the local heating "off"), a slow monotonous swelling occurs. After a certain time lag, the kinetics flips to a faster exponential dependency (with a time constant of 12 ± 1.7 ms). The transition phase occurs over the time span that prolongs when T_0 becomes close to the LCST (e.g., can be estimated as 25 ms for T_0 = 30 °C).

In the third experiment, the bulk temperature was adjusted below the LCST to T_0 = 23 °C, the local temperature increase was set to ΔT = 15 K, and the heating pulse duration was increased from t_p = 10 to 60 ms. The measured data in Figure 5c reveal that the collapsing kinetics can be fitted with a single exponential function (with a time constant of 6 ms) for short pulse length t_p up to 10–20 ms; however, above this time, a clear deviation occurs. For long heating pulses, the collapsing kinetics can be fitted as two overlaid exponential processes with time constants of 1.6 and 23.0 ms (see Supporting Information, section 3).

In order to elucidate the kinetics of the swelling and collapse of responsive hydrogels, a model based on the collective

https://doi.org/10.1021/acs.jpcb.2c01160
J. Phys. Chem. B 2022, 126, 3170–3179

diffusion of polymer chains is often used that was originally introduced by Tanaka et al. for responsive microgels[32] and later also adopted for other similar systems.[33,34] As illustrated in Figure 6a, the volumetric changes can be then described with a time-dependent displacement distance $u(x, t)$ for the investigated geometry of a thin layer that is allowed to swell only in the perpendicular direction to its surface and its changes follow the partial differential Fick-like diffusion equation

$$\frac{\partial u(x,\ t)}{\partial t} = \frac{\partial}{\partial x}\left[D\frac{\partial u(x,\ t)}{\partial x}\right] \tag{1}$$

where D is the collective diffusion coefficient. This coefficient is typically assumed to be constant and can be experimentally measured from dynamic light scattering experiments[35] or theoretically derived as a ratio of osmotic bulk modulus K and friction coefficient f.[33] Let us note that such picture holds only for small relative changes in $u(x, t)$ and that a range of effects taking place in the hydrogel layer is omitted including the dynamically changing inhomogeneities,[35] lateral stress leading to buckling effects,[36] and the impact of the attachment of the hydrogel to the arrays of Au nanoparticles that perturbed the (assumed) flat geometry.

In order to qualitatively explain some of the experimentally observed changes in the swelling and collapse when modulating the magnitude of the temperature stimulus ΔT and varying the ambient temperature T_0, let us take into account the dependence of the collective diffusion coefficient D on the Flory−Huggins parameter χ.[34] This parameter describes that the miscibility of the polymer with the solvent, here water, and for the studied thermo-responsive hydrogel is a function of temperature T.[37] The dependence of D on χ can be introduced by using the osmotic pressure Π description of Flory-like mean-field mixing energy with $K = \Phi\cdot\partial\Pi/\partial\Phi$,[33] (see Supporting Information, part 5) yielding a form of

$$D = A + B\chi\Phi(x,\ t)^2 = A - \frac{B'}{\left[1 + \frac{\partial u(x,\ t)}{\partial x}\right]^2} \tag{2}$$

where A, B, and B' are constants. Then, the diffusion coefficient is described as a function of the x coordinate and decreases (and thus slows down the swelling and collapse process) when the polymer volume fraction Φ increases. In addition, the thermo-responsiveness of the material can be captured based on the dependence of the Flory−Huggins parameter χ, enabling switching between a good solvent, that is, low χ, and a poor solvent, that is, high χ, regime.

Furthermore, let us analyze the time lag that was experimentally observed for the swelling process and that was absent in the collapsing process after the external stimulus was triggered [see Figure 5b]. By numerically solving the above-described partial differential eq 1 with appropriate boundary and initial conditions (see Supporting Information, part 6), we modeled the kinetics of the polymer volume fraction $\Phi(x, t)$ for the swelling and collapse and explored the impact of the dependence of collective diffusion coefficient D in form of eq 2. Let us note that then these simulations presented in Figure 6b,c can be related to the experimental data shown in Figure 5a−c as changes in Φ are directly proportional to the refractive index variations δn_h measured by LSPR at the inner interface of the hydrogel film (where $x = 0$).

As seen in the simulations results presented in Figure 6b, the swelling and collapse processes are predicted to show a similar exponential behavior when the collective diffusion coefficient D is set constant. However, the introduced dependence of D on the polymer volume fraction Φ in form of eq 2 leads to a different character of the swelling and collapse kinetics that can be ascribed to the effective decreasing of D in the zones with high Φ, which slows down both swelling and collapse processes in these regions. The collapse time dependence shows an exponential behavior as it occurs from the initially swollen hydrogel, which thus exhibits low Φ, and a corresponding high collective diffusion coefficient D. The reverse swelling process is different; it starts from compact collapsed hydrogel with low D, and the respective time dependence of the polymer volume fraction at the inner interface $\Phi(x = 0, t)$ is more complex and exhibits a pronounced delay with respect to the stimulus time. This behavior qualitatively agrees with the experimental observations in Figure 5b and suggests that for the studied system with strong changes in the swelling ratio, the effect of dependence of the collective diffusion coefficient on Φ cannot be omitted.

The origin of the delayed swelling process is illustrated by simulating the hydrogel density profile during the swelling process. The data presented in Figure 6c,d show the redistribution of the polymer volume fraction Φ in the gel layer as a function of the distance from the surface x and time t. They predict that for the constant D, the swelling process is associated with the Gaussian distribution of polymer volume fraction $\Phi(x)$ that rapidly changes with time through the whole layer. However, the proposed modification of D with introduced dependence on the Flory−Huggins parameter χ leads to slowing down of the swelling propagation from the outer to inner hydrogel interfaces. This effect leads to the pronounced offset in the swelling at the inner interface, which is not present for the collapse.

CONCLUSIONS

The obtained results reveal that the speed of swelling and collapsing of thermo-responsive polymer networks can, besides design of its chemical structure, be to a large extent controlled by the external parameters. As herein investigated for a micrometer-thick pNIPAAm hydrogel layer that is attached to a solid substrate, the response time of this network to an abrupt change in temperature (controlled on a time scale < 1 ms) substantially differs for the swelling and collapsing phases. The collapsing time scales with the difference between LCST and triggering (increased) temperature change and reaches a value as low as 1.5 ms. Interestingly, when the temperature pulse is prolonged, an additional slower collapsing transition with a characteristic time > 20 ms is overlaid, which has not been measured by a similar technique on non-cross-linked pNIPAAm polymer brushes.[22] The opposite transition from the collapsed to the swollen state is less affected by the magnitude of driving temperature change, and it occurs in two consecutive regimes. A time lag exceeding 20 ms is seen before the exponential transition to the swollen state proceeds with a time constant close to 10 ms. Based on the performed simulations, the time lag can be attributed to a potential gradient in the film that is due to the initial swelling at the outer interface (in contact with the solvent) propagating toward the optically probed inner interface (on the surface of the solid substrate). In general, these features indicate that the swelling and collapsing of small responsive hydrogel objects is

https://doi.org/10.1021/acs.jpcb.2c01160
J. Phys. Chem. B 2022, 126, 3170−3179

a complex process, and among others, it can provide advantage in design of recently emerged optically driven soft actuators and machines. Their considering may be important for systems researched to perform non-reciprocal morphing as a prerequisite for locomotion of soft micro-swimmers,[12] time-dependent switching between the hydrophobic and hydrophilic state can be utilized for construction of micro-crawlers,[6] or in design of responsive biointerfaces that allow rapid compacting of molecular species at plasmonic hotspots for subsequent sensitive plasmonically enhanced fluorescence spectroscopy detection.[30]

■ ASSOCIATED CONTENT

Supporting Information

The Supporting Information is available free of charge at https://pubs.acs.org/doi/10.1021/acs.jpcb.2c01160.

Calculation of the surface mass density of the hydrogel layers (PDF)

■ AUTHOR INFORMATION

Corresponding Author

Jakub Dostalek − *Biosensor Technologies, AIT-Austrian Institute of Technology GmbH, Tulln an der Donau 3430, Austria; Czech Academy of Sciences, FZU-Institute of Physics, Prague 182 21, Czech Republic;* orcid.org/0000-0002-0431-2170; Phone: +43 (0) 50550 4470; Email: jakub.dostalek@ait.ac.at; Fax: +43 (0) 50550 4450

Authors

Simone K. Auer − *Biosensor Technologies, AIT-Austrian Institute of Technology GmbH, Tulln an der Donau 3430, Austria; CEST Competence Center for Electrochemical Surface Technologies, Tulln an der Donau 3430, Austria;* orcid.org/0000-0001-7850-0302

Stefan Fossati − *Biosensor Technologies, AIT-Austrian Institute of Technology GmbH, Tulln an der Donau 3430, Austria;* orcid.org/0000-0002-1109-0035

Yevhenii Morozov − *Biosensor Technologies, AIT-Austrian Institute of Technology GmbH, Tulln an der Donau 3430, Austria;* orcid.org/0000-0001-9689-8641

Dario Cattozzo Mor − *Czech Academy of Sciences, FZU-Institute of Physics, Prague 182 21, Czech Republic;* orcid.org/0000-0002-4088-0116

Ulrich Jonas − *Macromolecular Chemistry, Department Chemistry-Biology, University of Siegen, Siegen 57076, Germany;* orcid.org/0000-0002-2161-4541

Complete contact information is available at: https://pubs.acs.org/10.1021/acs.jpcb.2c01160

Author Contributions

All authors have given approval to the final version of the paper.

Funding

Open Access is funded by the Austrian Science Fund (FWF).

Notes

The authors declare no competing financial interest.

■ ACKNOWLEDGMENTS

SA acknowledges support from FEMTECH, and YM is grateful for the support from the Austrian Science Fund (FWF) through the Lise Meitner Programme (M 2925). JD and SF were supported by the Austrian Science Fund through the project DIPLAB (I 5119). JD and DCM were supported by the Czech Science Fund through the project APLOMA (22-30456J).

■ ABBREVIATIONS

LSPR, localized surface plasmon resonance; pNIPAAm, poly(*N*-isopropylacrylamide); LCST, lower critical solution temperature;

■ REFERENCES

(1) Cao, X.; Lai, S.; James Lee, L. Design of a Self-Regulated Drug Delivery Device. *Biomed. Microdevices* **2001**, *3*, 109−118.

(2) Zhu, K.; Hou, D.; Fei, Y.; Peng, B.; Wang, Z.; Xu, W.; Zhu, B.; Li, L.-L.; Wang, H. Thermosensitive Hydrogel Interface Switching from Hydrophilic Lubrication to Infection Defense. *ACS Appl. Bio Mater.* **2019**, *2*, 3582−3590.

(3) Gisbert Quilis, N.; van Dongen, M.; Venugopalan, P.; Kotlarek, D.; Petri, C.; Moreno Cencerrado, A.; Stanescu, S.; Toca Herrera, J. L.; Jonas, U.; Möller, M.; et al. Actively Tunable Collective Localized Surface Plasmons by Responsive Hydrogel Membrane. *Adv. Opt. Mater.* **2019**, *7*, 1900342.

(4) Toma, M.; Jonas, U.; Mateescu, A.; Knoll, W.; Dostalek, J. Active Control of SPR by Thermoresponsive Hydrogels for Biosensor Applications. *J. Phys. Chem. C* **2013**, *117*, 11705−11712.

(5) Özkale, B.; Parreira, R.; Bekdemir, A.; Pancaldi, L.; Özelçi, E.; Amadio, C.; Kaynak, M.; Stellacci, F.; Mooney, D. J.; Sakar, M. S. Modular Soft Robotic Microdevices for Dexterous Biomanipulation. *Lab Chip* **2019**, *19*, 778−788.

(6) Rehor, I.; Maslen, C.; Moerman, P. G.; van Ravensteijn, B. G. P.; van Alst, R.; Groenewold, J.; Eral, H. B.; Kegel, W. K. Photo-responsive Hydrogel Microcrawlers Exploit Friction Hysteresis to Crawl by Reciprocal Actuation. *Soft Robot.* **2021**, *8*, 10−18.

(7) Roy, D.; Brooks, W. L. A.; Sumerlin, B. S. New Directions in Thermoresponsive Polymers. *Chem. Soc. Rev.* **2013**, *42*, 7214−7243.

(8) Mateescu, A.; Wang, Y.; Dostalek, J.; Jonas, U. Thin Hydrogel Films for Optical Biosensor Applications. *Membranes* **2012**, *2*, 40−69.

(9) Wang, Y.; Huang, C.-J.; Jonas, U.; Wei, T.; Dostalek, J.; Knoll, W. Biosensor Based on Hydrogel Optical Waveguide Spectroscopy. *Biosens. Bioelectron.* **2010**, *25*, 1663−1668.

(10) Aulasevich, A.; Roskamp, R. F.; Jonas, U.; Menges, B.; Dostálek, J.; Knoll, W. Optical Waveguide Spectroscopy for the Investigation of Protein-Functionalized Hydrogel Films. *Macromol. Rapid Commun.* **2009**, *30*, 872−877.

(11) Yin, J.; Li, C.; Wang, D.; Liu, S. FRET-Derived Ratiometric Fluorescent K+ Sensors Fabricated from Thermoresponsive Poly(N -Isopropylacrylamide) Microgels Labeled with Crown Ether Moieties. *J. Phys. Chem. B* **2010**, *114*, 12213−12220.

(12) Mourran, A.; Jung, O.; Vinokur, R.; Möller, M. Microgel That Swims to the Beat of Light. *Eur. Phys. J. B* **2021**, *44*, 79.

(13) Nishiguchi, A.; Zhang, H.; Schweizerhof, S.; Schulte, M. F.; Mourran, A.; Möller, M. 4D Printing of a Light-Driven Soft Actuator with Programmed Printing Density. *ACS Appl. Mater. Interfaces* **2020**, *12*, 12176−12185.

(14) Dong, L.; Agarwal, A. K.; Beebe, D. J.; Jiang, H. Adaptive Liquid Microlenses Activated by Stimuli-Responsive Hydrogels. *Nature* **2006**, *442*, 551−554.

(15) Gao, W.; Dong, R.; Thamphiwatana, S.; Li, J.; Gao, W.; Zhang, L.; Wang, J. Artificial Micromotors in the Mouse's Stomach: A Step toward in Vivo Use of Synthetic Motors. *ACS Nano* **2015**, *9*, 117−123.

(16) Sershen, S. R.; Mensing, G. A.; Ng, M.; Halas, N. J.; Beebe, D. J.; West, J. L. Independent Optical Control of Microfluidic Valves Formed from Optomechanically Responsive Nanocomposite Hydrogels. *Adv. Mater.* **2005**, *17*, 1366−1368.

(17) Mourran, A.; Zhang, H.; Vinokur, R.; Möller, M. Soft Microrobots Employing Nonequilibrium Actuation via Plasmonic Heating. *Adv. Mater.* **2017**, *29*, 1604825.

(18) Ding, T.; Valev, V. K.; Salmon, A. R.; Forman, C. J.; Smoukov, S. K.; Scherman, O. A.; Frenkel, D.; Baumberg, J. J. Light-Induced Actuating Nanotransducers. *Proc. Natl. Acad. Sci. U. S. A.* **2016**, *113*, 5503−5507.
(19) Gallagher, S.; Florea, L.; Fraser, K.; Diamond, D. Swelling and Shrinking Properties of Thermo-Responsive Polymeric Ionic Liquid Hydrogels with Embedded Linear PNIPAAM. *Int. J. Mol. Sci.* **2014**, *15*, 5337−5349 Vol. 15, Pages 5337-5349.
(20) Winkler, P.; Belitsch, M.; Tischler, A.; Häfele, V.; Ditlbacher, H.; Krenn, J. R.; Hohenau, A.; Nguyen, M.; Félidj, N.; Mangeney, C. Nanoplasmonic Heating and Sensing to Reveal the Dynamics of Thermoresponsive Polymer Brushes. *Appl. Phys. Lett.* **2015**, *107*, 141906.
(21) Govorov, A. O.; Zhang, W.; Skeini, T.; Richardson, H.; Lee, J.; Kotov, N. A. Gold Nanoparticle Ensembles as Heaters and Actuators: Melting and Collective Plasmon Resonances. *Nanoscale Res. Lett.* **2006**, *1*, 84−90.
(22) Nguyen, M.; Sun, X.; Lacaze, E.; Winkler, P. M.; Hohenau, A.; Krenn, J. R.; Bourdillon, C.; Lamouri, A.; Grand, J.; Lévi, G.; et al. Engineering Thermoswitchable Lithographic Hybrid Gold Nanorods as Plasmonic Devices for Sensing and Active Plasmonics Applications. *ACS Photonics* **2015**, *2*, 1199−1208.
(23) Liu, G.; Zhang, G. Collapse and Swelling of Thermally Sensitive Poly (N-Isopropylacrylamide) Brushes Monitored with a Quartz Crystal Microbalance. *J. Phys. Chem. B* **2005**, *109*, 743−747.
(24) Gisbert Quilis, N.; Lequeux, M.; Venugopalan, P.; Khan, I.; Knoll, W.; Boujday, S.; Lamy de la Chapelle, M.; Dostalek, J. Tunable Laser Interference Lithography Preparation of Plasmonic Nanoparticle Arrays Tailored for SERS. *Nanoscale* **2018**, *10*, 10268−10276.
(25) Sergelen, K.; Petri, C.; Jonas, U.; Dostalek, J. Free-Standing Hydrogel-Particle Composite Membrane with Dynamically Controlled Permeability. *Biointerphases* **2017**, *12*, 051002.
(26) Beines, P. W.; Klosterkamp, I.; Menges, B.; Jonas, U.; Knoll, W. Responsive Thin Hydrogel Layers from Photo-Cross-Linkable Poly(N-Isopropylacrylamide) Terpolymers. *Langmuir* **2007**, *23*, 2231−2238.
(27) Petri, C. Synthesis and Characterization of Novel Photo-Crosslinkable Poly (2-Oxazoline)-Based Hydrogel Systems for the Application as Biosensor Matrix, Ph.D. Thesis, 2018.
(28) Johnson, P. B.; Christy, R. W. Optical Constants of the Noble Metals. *Phys. Rev. B* **1972**, *6*, 4370.
(29) Johnson, P.; Christy, R. Optical Constants of Transition Metals: Ti, V, Cr, Mn, Fe, Co, Ni, and Pd. *Phys. Rev. B* **1974**, *9*, 5056.
(30) Hageneder, S.; Jungbluth, V.; Soldo, R.; Petri, C.; Pertiller, M.; Kreivi, M.; Weinhäusel, A.; Jonas, U.; Dostalek, J. Responsive Hydrogel Binding Matrix for Dual Signal Amplification in Fluorescence Affinity Biosensors and Peptide Microarrays. *ACS Appl. Mater. Interfaces* **2021**, *13*, 27645−27655.
(31) Baffou, G.; Berto, P.; Bermúdez Ureña, E.; Quidant, R.; Monneret, S.; Polleux, J.; Rigneault, H. Photoinduced Heating of Nanoparticle Arrays. *ACS Nano* **2013**, *7*, 6478−6488.
(32) Tanaka, T.; Sato, E.; Hirokawa, Y.; Hirotsu, S.; Peetermans, J. Critical Kinetics of Volume Phase Transition of Gels. *Phys. Rev. Lett.* **1985**, *55*, 2455.
(33) Jia, D.; Muthukumar, M. Theory of Charged Gels: Swelling, Elasticity, and Dynamics. *Gels* **2021**, *7*, 49 Page 49 2021.
(34) Toomey, R.; Vidyasagar, A.; Ortiz, O. Swelling Behavior of Thin Hydrogel Coatings. *Funct. Polym. Films* **2011**, *2*, 649−667.
(35) Gianneli, M.; Roskamp, R. F.; Jonas, U.; Loppinet, B.; Fytas, G.; Knoll, W. Dynamics of Swollen Gel Layers Anchored to Solid Surfaces. *Soft Matter* **2008**, *4*, 1443−1447.
(36) Sultan, E.; Boudaoud, A. The Buckling of a Swollen Thin Gel Layer Bound to a Compliant Substrate. *J. Appl. Mech.* **2008**, *75*, 0510021−0510025.
(37) Erman, B.; Flory, P. J. Critical Phenomena and Transitions in Swollen Polymer Networks and in Linear Macromolecules. *Macromolecules* **2002**, *19*, 2342−2353.

https://doi.org/10.1021/acs.jpcb.2c01160
J. Phys. Chem. B 2022, 126, 3170−3179